

CHARACTERIZATION OF PHOTONIC CRYSTALS AT  
MICROWAVE FREQUENCIES

A THESIS  
SUBMITTED TO THE DEPARTMENT OF PHYSICS  
AND THE INSTITUTE OF ENGINEERING AND SCIENCE  
OF BILKENT UNIVERSITY  
IN PARTIAL FULFILLMENT OF THE REQUIREMENTS  
FOR THE DEGREE OF  
MASTER OF SCIENCE

By  
Burak Temelkuran  
September 1996

THESIS

QC  
793.5  
·P427  
T46  
1996

# CHARACTERIZATION OF PHOTONIC CRYSTALS AT MICROWAVE FREQUENCIES

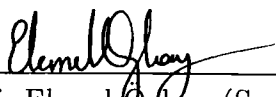
A THESIS  
SUBMITTED TO THE DEPARTMENT OF PHYSICS  
AND THE INSTITUTE OF ENGINEERING AND SCIENCE  
OF BİLKENT UNIVERSITY  
IN PARTIAL FULFILLMENT OF THE REQUIREMENTS  
FOR THE DEGREE OF  
MASTER OF SCIENCE

By  
Burak Temelkuran  
September 1996

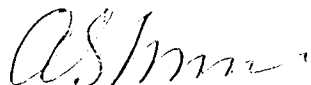
B.035237

QC  
793.5  
.P427  
T46  
1996

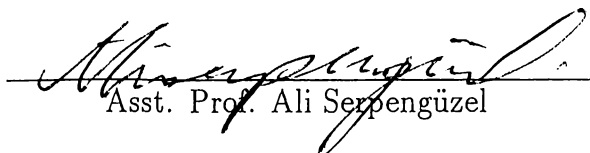
I certify that I have read this thesis and that in my opinion it is fully adequate, in scope and in quality, as a dissertation for the degree of Master of Science.

  
Asst. Prof. Ekmel Ozbay (Supervisor)

I certify that I have read this thesis and that in my opinion it is fully adequate, in scope and in quality, as a dissertation for the degree of Master of Science.

  
Prof. Alexander Shumovsky

I certify that I have read this thesis and that in my opinion it is fully adequate, in scope and in quality, as a dissertation for the degree of Master of Science.

  
Asst. Prof. Ali Serpengüzel

Approved for the Institute of Engineering and Science:

  
Prof. Mehmet Baray  
Director of Institute of Engineering and Science

# Abstract

## CHARACTERIZATION OF PHOTONIC CRYSTALS AT MICROWAVE FREQUENCIES

Burak Temelkuran

M. S. in Physics

Supervisor: Asst. Prof. Ekmel Özbay

September 1996

We investigated the surface reflection properties of layer-by-layer photonic crystals, for dielectric and metallic based photonic crystals. By using a Fabry-Perot cavity analogy with the reflection-phase information of the photonic crystals, we predicted defect frequencies of planar defect structures. Our predictions were in good agreement with the measured defect frequencies. The Fabry-Perot cavity analogy was also used to relate the quality factors of the planar defect structures to the transmission of the mirrors of the cavity. A simple model was used to simulate the transmission spectra of planar defect structures, which agreed well with the experimental data. We also investigated the transmission and reflection properties of two different metallic crystal structures (face-centered-tetragonal and simple tetragonal). We obtained rejection rates of 7-8 dB per layer from metallic crystals. Defect modes created by removing rods resulted in high peak transmission (80%), and high quality factors (1740). Our measurements were in good agreement with theoretical simulations of metallic structures. Planar defect structures built around metallic structures resulted in higher quality factors (2250). We observed high reflection-rejection ratios (-80 dB) at defect frequencies

for planar defect structures, which was explained by using the Fabry-Perot analogy. Finally, the enhanced field inside the defect volume was measured, by using a monopole receiver antenna inserted inside the defect. The maximum observed enhancement with respect to the incident field was around 200 for a planar defect structure. By placing a Schottky diode detector inside planar and box-like defects, we built resonant cavity enhanced (RCE) detectors and measured the enhanced field inside the defect.

**Keywords:** Photonic Crystals, Fabry-Perot Cavity, Planar Defects, Localized Defects, Quality Factor, Optical Field Enhancement, Schottky Diode Detector, Metallic Photonic Crystal, Resonant Detector, Reflection-Phase Measurement.

# Özet

## MİKRODALGA FREKANSLARINDA FOTONİK KRİSTALLERİN KARAKTERİZASYONU

Burak Temelkuran

Fizik Yüksek Lisans

Tez Yöneticisi: Asst. Prof. Ekmel Özbay

Eylül 1996

Katmanlardan oluşan fotonik kristallerin yüzey yansıtma özelliklerini, dielektrik ve metal kristaller için inceledik. Fabry-Perot çınlaç benzeşimini fotonik kristallerin yansıtma-fazı bilgisi ile birlikte kullanarak, düzlemsel düzensizlik yapılarının rezonans frekanslarını tahmin ettiğim. Kuramsal tahminlerimiz, ölçülen rezonans frekanslarına uyuyordu. Fabry-Perot çınlaç benzeşimi, düzlemsel düzensizlik yapılarının kalite faktörleriyle çınlacın aynalarının geçirgenliği arasında bir ilişki kurmak için de kullanıldı. Düzlemsel düzensizlik yapılarının geçirgenlik spektrumunu simüle etmek için, sonuçları deneysel verilerle uyuşan basit bir model kullanıldı. İki ayrı metalik kristal yapısının (basit tetragonal ve yüzmerkezli-tetragonal) geçirgenlik ve yansıtma özellikleri incelendi. Metalik kristallerden katman başına 7-8 dB sinyal düşüşleri elde edildi. Çubukların çıkarılması ile oluşturulan rezonans modları, yüksek değerde tepe geçirgenliği (%80) ve yüksek kalite faktörleri (1740) ile sonuçlandı. Ölçümlerimiz ile metalik yapıların kuramsal simülasyonları birbirini tutuyordu. Metalik yapılarda oluşturulan düzlemsel düzensizliklerin kalite faktörleri daha yükseldi (2250). Bunun yanında, düzlemsel düzensizliklerin rezonans frekanslarında yüksek

oranlarda yansıtma-reddi gözlendi (-80 dB), ve bu olay Fabry-Perot benzeşimi ile açıklandı. Son olarak, tek kutupsal bir anten alıcı olarak kullanılarak, düzensizliğin içinde kuvvetlendirilmiş alan ölçümleri yapıldı. Gözlemlenen en büyük kazanç, sinyalin, gönderilen sinyale göre yaklaşık 200 kat kadar artmasıydı. Düzlemsel ve kutu benzeri düzensizliklerin içine Schottky diyot algılayıcıları yerleştirilerek, rezonans çinlaç ile kuvvetlendirilmiş bir algılayıcı yapıldı ve düzensizlik içerisindeki kuvvetlendirilmiş alan ölçüldü.

## Anahtar

**sözcükler:** Fotonik Kristaller, Fabry-Perot Çinlacı, Kristal Düzensizliği, Kalite Faktörü, Optik Alan Kazancı, Schotky Diyot Detektör, Metalik Fotonik Kristaller, Rezonans Algılayıcı, Yansıtma-Faz Ölçümleri.

# Acknowledgement

I would like to express my gratitude to my thesis supervisor Prof. Ekmel Özbay for his invaluable guidance and motivation during my graduate study. I'd also like to thank Prof. M. Sigalas and Prof. K.M. Ho from ISU, for helping me with their simulations. I am also grateful to the members of the Department of Physics, Bilkent University, for valuable discussions and comments. I also thank all of my friends, who supplied me continuous morale support, and especially Canan, who decided to spend all her life with me.

# Contents

<b>Abstract</b>	i
<b>Özet</b>	iii
<b>Acknowledgement</b>	v
<b>Contents</b>	vi
<b>List of Figures</b>	viii
<b>1 Introduction</b>	1
1.1 Motivation . . . . .	2
1.2 History . . . . .	4
1.3 Defect Structures and Doping . . . . .	6
1.4 Antennas	9
1.5 Waveguides . . . . .	11
1.6 Metallic photonic crystals and other applications . . . . .	12
1.7 Summary of this work	12
<b>2 Reflection Properties and Defect Formation</b>	14
2.1 Defect structures . . . . .	14
2.2 Reflection measurements . . . . .	17
2.3 Fabry-Perot analogy	18
2.4 Quality Factor . . . . .	23

<b>3</b>	<b>Metallic Photonic Crystals</b>	<b>27</b>
3.1	Structure . . . . .	27
3.2	Transmission properties	29
3.3	Defect structures . . . . .	32
3.4	Reflection properties and Fabry-Perot type cavities in metallic structures . . . . .	41
<b>4</b>	<b>Resonant Detectors Inside Dielectric Photonic Crystals</b>	<b>46</b>
4.1	The circulating intensity magnification . . . . .	47
4.2	Experimental setup . . . . .	50
4.3	Measurements . . . . .	52
<b>5</b>	<b>Conclusions</b>	<b>59</b>

# List of Figures

1.1	Inhibition of spontaneous emission. . . . .	3
1.2	The drilling technique used in the construction of the first photonic crystal that possessed 3-D PBG. . . . .	5
1.3	Layer-by-layer structure . . . . .	7
1.4	Sample defect transmission characteristics. . . . .	8
1.5	Antenna applications . . . . .	10
1.6	Waveguide carved inside a 1-D photonic crystal. . . . .	11
2.1	Experimental setup . . . . .	15
2.2	Reflection and transmission characteristics . . . . .	16
2.3	Transmission from a single rod removed defect structure	16
2.4	Phase information . . . . .	17
2.5	High Q factor defect mode. . . . .	19
2.6	Phase comparison . . . . .	21
2.7	Double defect . . . . .	22
2.8	Inverse Q factor and Transmission . . . . .	24
2.9	Comparison of defect theory with experiment	25
3.1	Two types of layer-by-layer photonic crystals . . . . .	28
3.2	The transmission characteristics of fct and st metallic structures .	30
3.3	Transmission from 10-layer metallic photonic crystal . . . . .	31
3.4	Transmission at different angle of incidences. . . . .	32
3.5	Comparison of the transmission characteristics of defect structures of st and fct crystals. . . . .	33
3.6	Transmission Characteristics of an st 18-Layer Defect. . . . .	35

3.7	Comparison of Theoretical and Experimental results of a Defect Mode . . . . .	36
3.8	Defect mode with a high Q-factor. . . . .	37
3.9	Comparison of experimental peak amplitudes of defect modes with the theory. . . . .	38
3.10	The additional peaks observed for the planar defect structure.	40
3.11	Reflection and transmission characteristics of st crystal . . . . .	41
3.12	The reflection-phase information. . . . .	42
3.13	Phase Comparison of Theory and Experiment (1). . . . .	43
3.14	Phase Comparison of Theory and Experiment (2). . . . .	43
3.15	High reflection rejection from a defect structure. . . . .	45
4.1	Magnification of the circulating signal.	48
4.2	Fabry-Perot modeling . . . . .	49
4.3	RCE modeling . . . . .	50
4.4	Experimental setup . . . . .	51
4.5	Defect Structure . . . . .	52
4.6	Transmission spectra of a defect mode	53
4.7	Power enhancement of a defect mode . . . . .	54
4.8	Enhancement of the field inside a planar defect. . . . .	55
4.9	Transmission spectra from a box-like cavity. . . . .	56
4.10	Circulating intensity magnification inside a box like cavity (1). . .	56
4.11	Circulating intensity magnification inside a box like cavity (2). . .	57

# Chapter 1

## Introduction

Electrons in a crystal have energy bands that are separated by forbidden regions, which are called electronic band gaps. In these regions, wavelike electron orbitals are not allowed. The basic reason behind the band structure, is the periodicity of the potential within the crystal. On the other hand, for photons, a material with a periodically changing dielectric constant may also result in a similar band structure. Using this analogy, the first photonic band gap (PBG) crystal was proposed by Eli Yablonovitch in 1987.<sup>1</sup> The main goal is to have a frequency band in which the propagation of the electromagnetic waves are forbidden for every direction. So what we call a photonic crystal is a periodically arranged structure, where air or dielectric material has lattice-like behavior. Such a PBG crystal reflects the propagating electromagnetic (EM) waves in all directions due to Bragg-scattering conditions. We can easily see this analogy in the equations of a propagating electron wave in a space-variant potential  $V(\mathbf{r})$  (1.1), and the propagation of EM waves in a dielectric media with a space-variant dielectric function for the electric field amplitude  $\mathbf{E}(\mathbf{r})$  (1.2).<sup>2</sup>

$$\left\{ -\frac{\hbar^2}{2m^*} \nabla^2 + V(\mathbf{r}) \right\} \Psi(\mathbf{r}) = E\Psi(\mathbf{r}) \quad (1.1)$$

$$\left\{ -\nabla^2 - \frac{\omega^2}{c^2} \epsilon_{fluct}(\mathbf{r}) \right\} \mathbf{E}(\mathbf{r}) + \nabla (\nabla \cdot \mathbf{E}(\mathbf{r})) = \epsilon_0 \frac{\omega^2}{c^2} \mathbf{E}(\mathbf{r}) \quad (1.2)$$

In equation 1.1,  $\hbar$  is the Planck constant divided by  $2\pi$ ,  $m^*$  is the effective electron mass, and  $\Psi(\mathbf{r})$  is the scalar wave function. In the second equation,  $\omega$  is the angular frequency of the field, and  $c$  is the speed of light in free space. Except the term  $\nabla(\nabla \cdot \mathbf{E})$ , the analogy between the Schrödinger equation (1.1) and the Maxwell equation (1.2) is obvious. The total dielectric constant in the second equation is separated as  $\epsilon(\mathbf{r}) = \epsilon_0 + \epsilon_{fluct}(\mathbf{r})$ , into its average value  $\epsilon_0$  and a spatially fluctuating part  $\epsilon_{fluct}(\mathbf{r})$ . The latter plays a role analogous to the  $V(\mathbf{r})$  in the Schrödinger equation, and the quantity  $\epsilon_0 \frac{\omega^2}{c^2}$  plays the role of the energy eigenvalue  $E$  of the Schrödinger equation.

The PBG idea has led to proposals for many novel applications at optical wavelengths, such as thresholdless lasers<sup>3</sup> and efficient single mode light emitting diodes.<sup>4,5</sup> These applications are later extended to microwave and millimeter wave regime, such as efficient reflectors, millimeter wave antennas, filters, sources, and waveguides.<sup>6,7,8,9</sup> As a result, there have been a great deal of interest in this research subject during the last few years.

## 1.1 Motivation

The control of spontaneous emission plays an important role in many applications based on quantum electronics and quantum optics. Many corresponding examples can be found. The threshold of a laser, the current gain in heterojunction bipolar transistors, and the maximum available output voltage in solar cells, all depend on the spontaneous recombination of electrons and holes.<sup>10</sup>

Before 1980's, spontaneous emission was known to be a natural phenomena which could not be controlled. Later, it was found that spontaneous emission could be reduced inside a metallic waveguide, where no propagation mode is allowed up to a certain cut-off frequency.<sup>11</sup> But as metals absorb most of the EM waves at optical frequencies, this method is not feasible at optical wavelengths. On the other hand, dielectric materials or insulators may be used to overcome this absorption problem. So dielectric based photonic crystals which do not allow propagation of EM waves can also be used to inhibit spontaneous emission.

Figure 1.1 shows how the spontaneous emission can be controlled by a photonic crystal.<sup>10</sup> In a semiconductor, a photon is emitted by the recombination of an electron in the valence band with a hole in the conduction band. However, if the photonic crystal is designed to have a band gap covering the frequency of the emission, the photon will have no mode to couple, and the recombination will simply be inhibited.

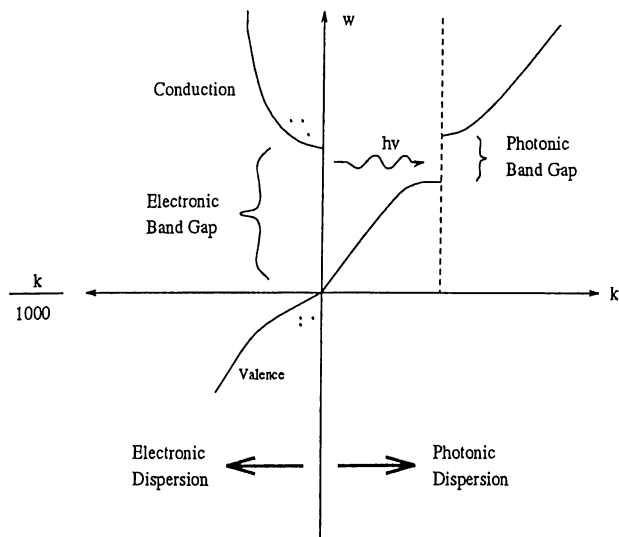


**Figure 1.1:** Inhibition of spontaneous emission.

Right side, the dispersion relation for the EM waves, left side, the dispersion relation for electron waves of a typical direct-gap semiconductor.

An example can clarify the use of this idea. Yamamoto was able to limit the noise in an electrical current flow by a good quality metal film resistor, and drove a high-quantum efficiency-laser diode with this resistor.<sup>12</sup> Assuming a 100% efficient laser, a single photon would be produced for every single electron. With this design, a photon could be used as a single communication unit. However the problem was to achieve such a highly efficient laser. If the typical amount of random spontaneous emission captured by the cavity of the laser were to be around 50%, then the signal to noise ratio (SNR) would only be 3 dB. This SNR is quite low, and should be increased. Using a photonic crystal, spontaneous emission could be reduced to 1%. That would correspond to a 20 dB SNR, which

is a highly desirable value.

It should be noted that the idea of PBG is different from the concept of one-dimensional stop bands used in electrical engineering. Rather, the photonic crystals are expected to have stop bands in all directions. Early studies made on X-ray diffractions from natural fcc crystals showed narrow stop bands.<sup>10</sup> This idea acted as the basis in the development of the PBG theories. But due to the refractive-index difference between vacuum and matter being low, the stop bands that are observed were narrow. Calculations showed that with refractive-index difference higher than 2, these stop bands may be opened to cover all directions in reciprocal space.<sup>13</sup>

## 1.2 History

Photonic crystals which would be functional at optical frequencies require submicron dimensions. However, due to the difficulties in fabrication, people first tried to construct crystals at larger dimensions suitable for microwave characterization (15 GHz). The early PBG studies concentrated on testing various fcc type fabricated crystals. The reason for choosing fcc type crystals was their Brillouin zone being close to a sphere. Otherwise, the  $\mathbf{k}$  vectors along different directions would differ in magnitude, and corresponding gaps would not overlap. In one of the early tries, fcc type of periodicity for the spherical dielectric atoms was chosen,<sup>1</sup> where the dielectric constant of these spherical atoms was 3.06. These were embedded inside a blue foam material of dielectric constant near unity. Another crystal was fabricated by Yablonovitch *et al* by drilling techniques.<sup>14</sup> It was a spherical-void structure with oversized voids breaking through the walls of Wigner-Seitz (WS) unit cells. Although theories of that time predicted that the second crystal should possess a PBG in all directions, both crystals failed to produce a stop band. The reason behind this failure was the treatment of the EM field as a scalar field as in Schrödinger's approach, which resulted in wrong predictions.

By the introduction of vector wave calculations, scientists proved that the

early structures did not have a full band gap due to band crossing along W direction of the Brillouin zone.<sup>15,16</sup> The problem of band crossing was solved by a diamond structure suggested by the Iowa State group of Ho *et al.*<sup>13</sup> This predicted structure was later fabricated by drilling a solid dielectric material from three different angles, each 35.26° away from the normal and spread 120° on the azimuth.<sup>17</sup> The crystal in the end was a full 3-D fcc structure with roughly cylindrical void atoms. This was the first experimental photonic crystal that possessed 3-D stop band. Along ⟨111⟩ direction, a gap extending from 13 GHz to 16 GHz was observed, with around 50 dB attenuation.

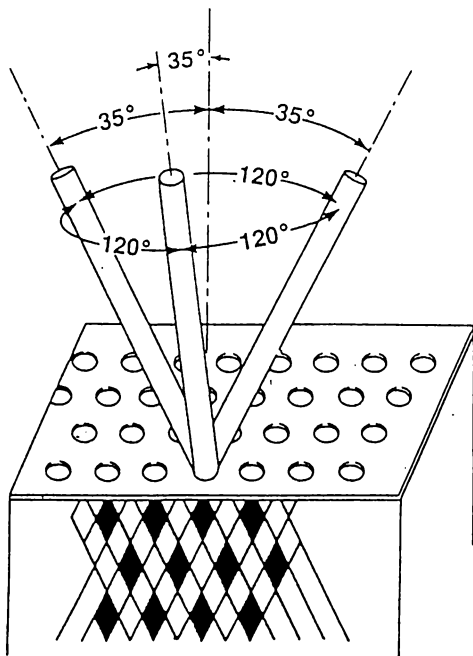


Figure 1.2: The drilling technique used in the construction of the first photonic crystal that possessed 3-D PBG.

After this verification of the existence of photonic crystals, there was an increased effort in this research area. Scientists searched for new structures that could be more easily fabricated, and could be scaled down to optical frequencies. A new crystal that meets these requirements was invented by the Iowa State group.<sup>18</sup> The designed structure, which was called layer-by-layer photonic crystal, has 3-D PBG, and could also easily be scaled to lower dimensions. Each layer of crystal was formed by dielectric rods arranged parallel to each other separated

by a distance  $a$ . As seen in figure 1.3, each layer is stacked to the previous one by rotating the layer  $90^\circ$  with respect to the previous layer. Every third layer is parallel to the first one with a shift of  $a/2$  in the direction perpendicular to the rods. The fourth layer is shifted the same way with respect to the second layer. So a unit cell of 4 layers of length  $c$ , where every fifth layer repeats the first one, is obtained. The angle between adjacent layers may vary from  $90^\circ$  to  $60^\circ$ . The structure has the symmetry of a face centered tetragonal (fct) type of structure. The crystal can be derived from a diamond structure if 110 chains of atoms were to be replaced by dielectric rods for the special case of  $c/a=\sqrt{2}$ .

This structure is important in the sense that, its dimensions could easily be lowered. Using the anisotropic etching property of Si by KOH, the layers of these crystals were prepared by micromachining techniques at lower scales. First a gap around 100 GHz was reached.<sup>19</sup> Then the dimensions were further scaled down to achieve a photonic crystal with a full band gap around 500 GHz.<sup>20</sup> By using special silicon thinning methods and double etching the wafers from both faces, this technique could be extended to have photonic band gaps around 3 THz.<sup>21</sup>

### 1.3 Defect Structures and Doping

Similar to the doping of semiconductor crystals, localized electromagnetic modes can be produced in photonic crystals by introducing defects that break the symmetry of the crystal.<sup>22</sup> This can be achieved by two different methods. First, we can add extra dielectric material to the crystal, which acts like a donor atom in a semiconductor. Second, we can remove some part of the dielectric material from the crystal, which acts like an acceptor atom. Experiments show that the acceptor modes, acting like microresonator cavities, are of greater importance with their highly localized and single mode cavity characteristics.<sup>22,23</sup> These localized modes within the band gap are observed in previously mentioned photonic crystals. As an example, a defect structure can be produced by removing a part or all of a single rod from a single layer in a layer by layer structure. The transmission profile does not change from that of the core crystal. The only change is in the

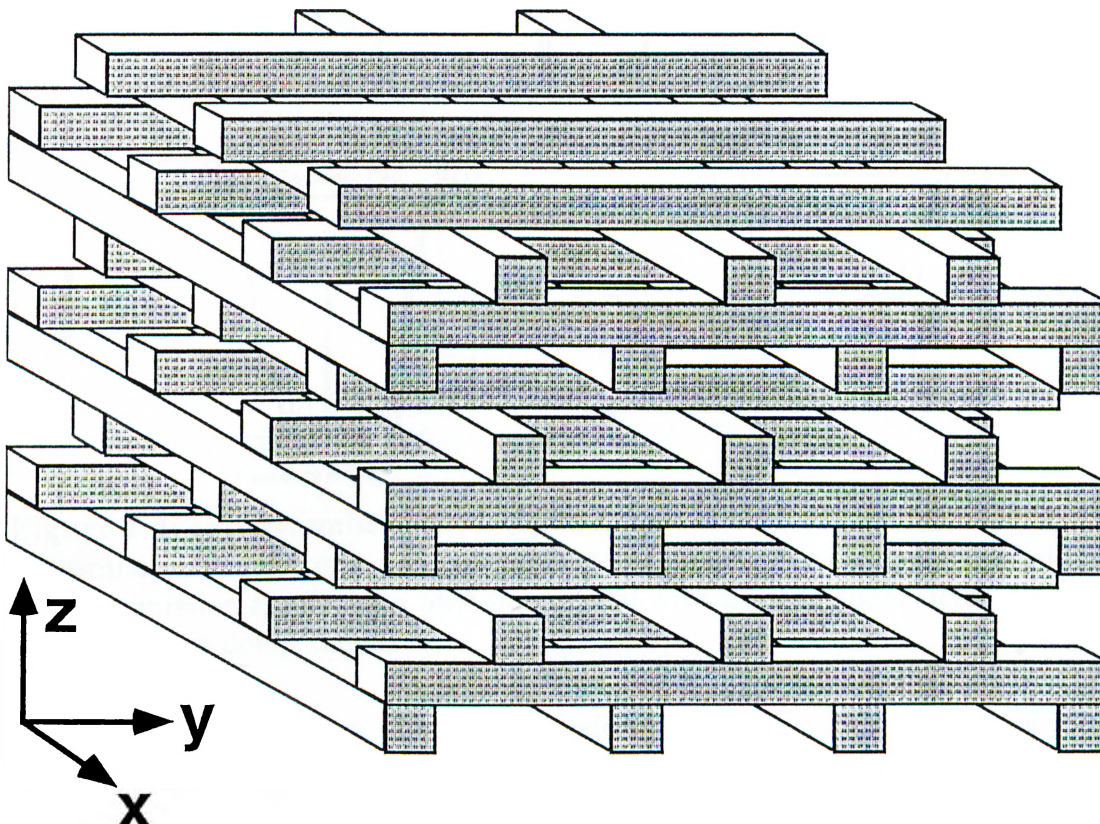


**Figure 1.3:** Layer-by-layer structure

The design of an fct type of layer-by-layer crystal with a 3-D PBG. The structure is built by an orderly stacking of dielectric rods.

localized mode frequency, where a transmission peak appears inside the gap. The experimentally observed Q factors (quality factor, defined as the center frequency divided by the peak's full width at half maximum) of these localized modes were around 1000-2000, while the theory expected to have high Q factors of the order of  $10^6$  for such defect structures.<sup>23</sup> The finite size of the crystal and the material absorption were the main reasons for this significant difference.

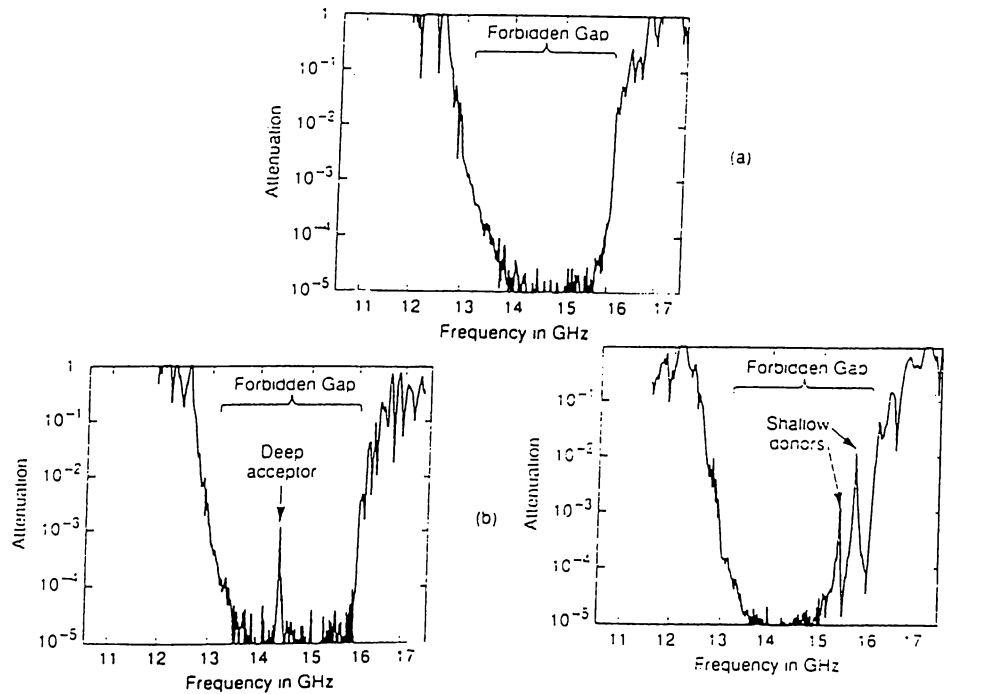


**Figure 1.4:** (a) Transmission attenuation from a defect free photonic crystal. (b) Transmission spectra of a photonic crystal with a single acceptor in the middle. (c) Transmission spectra of a photonic crystal with a single donor defect, leading to two shallow donor modes.<sup>10</sup>

With the introduction of localized modes, photonic crystals can be used in a variety of applications. The spontaneous emission was controlled by forbidding the propagation at a range of frequencies by the core crystal. By the introduction of a defect, a single frequency can be adjusted to allow stimulated emission. By this way, the coupling coefficient of spontaneous emission into stimulated emission could be increased from  $10^{-5}$  to approximately 1 in a semiconductor laser. This would mean thresholdless lasers, which are well worth fighting for.<sup>3</sup> A similar approach can be used to achieve single mode light emitting diodes (SM-LED). The coupling coefficient of spontaneous emission to that of the desired single mode is very low in an SM-LED. The defect frequency of the photonic crystal can be arranged to match the single mode operating frequency of the diode. This would increase the coupling coefficient, up to unity.<sup>4,5</sup>

These were the major motivations of the photonic crystals in the beginning. However, the possible applications in the area went far beyond the expectations.

Many applications came into view with the work done at microwave and millimeter wave frequencies. The most important ones are efficient antennas on photonic crystals and waveguide applications.

## 1.4 Antennas

Photonic crystals can also be implemented in the area of signal propagation and control. Antenna applications are good examples for this approach. In microwave and millimeter-wave integrated circuits, the control of the radiation from a dipole antenna is of great importance. In such circuits, the antenna is mounted on a semiconductor substrate, which enhances the performance and functionality of the circuit. But most of the power from the antenna on a dielectric substrate is radiated into the substrate. The ratio of the power radiated into the substrate, to the power radiated into air is  $\epsilon^{1.5}$ , where  $\epsilon$  is the dielectric constant of the substrate. As an example, a dipole antenna on a GaAs substrate emits 46 times more power into the substrate than into the air. Also the radiated waves, which have angle of incidence greater than the critical angle, are trapped inside the substrate due to total internal reflection (figure 1.5). Since this critical angle in GaAs is a small value, around  $16^\circ$ , a big percentage of the field is trapped. As a result, standard antennas on GaAs or Si radiate only 2-3% of their power into air. If a thin substrate is used to overcome the loss due to this trapping, another problem arises. A  $180^\circ$  phase shift comes from the reflection at the bottom conductor, resulting the radiation to cancel out at driving point. These problems can be solved, if the antenna was to be mounted on a 3-D photonic crystal, from which the radiation will fully be reflected in all directions. Since the reflections occur due to the Bragg scatterings, the phase shift of the reflected field won't cancel out the radiated one. People use metallic feedhorns, which are more efficient than dielectric structures, at frequencies above 20 GHz. But the problem with these antennas is that the reflection occurs only on the surface of a metal. So all the power lost is converted to heat on the surface, causing overheating in a very small volume. Whereas in photonic crystals, the reflections

occur within at least a unit cell, which is much longer than the skin depth of the metals. As a result, the heat is distributed over a large volume, which would enable a lower operating temperature. Experiments done by mounting a dipole antenna on a photonic crystal shows that nearly all the field is radiated into air, which proves the usefulness of this idea.<sup>6,7,24</sup>

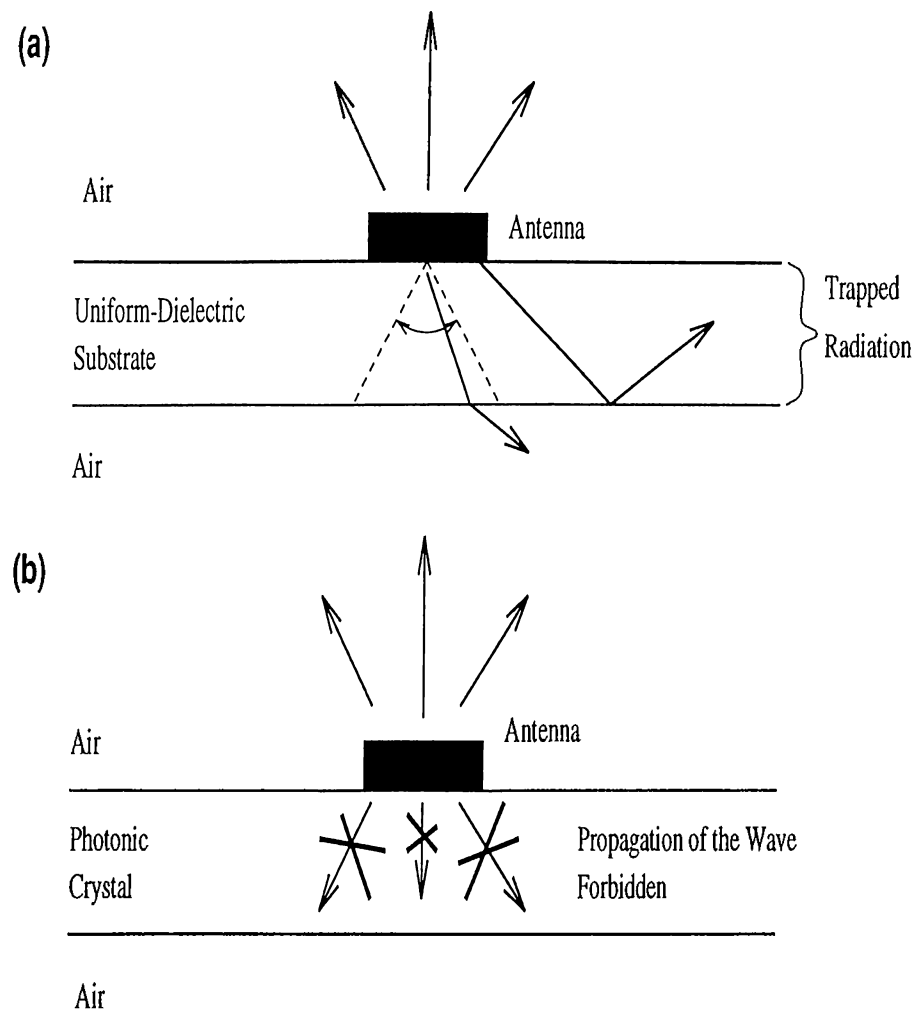


**Figure 1.5:** Antenna applications

(a) Antenna mounted on a semiconductor substrate. Most of the power goes into the substrate, and also trapped inside it. (b) Antenna on a photonic crystal. The crystal fully reflects the radiated field. The radiated field is directed and enhanced.

## 1.5 Waveguides

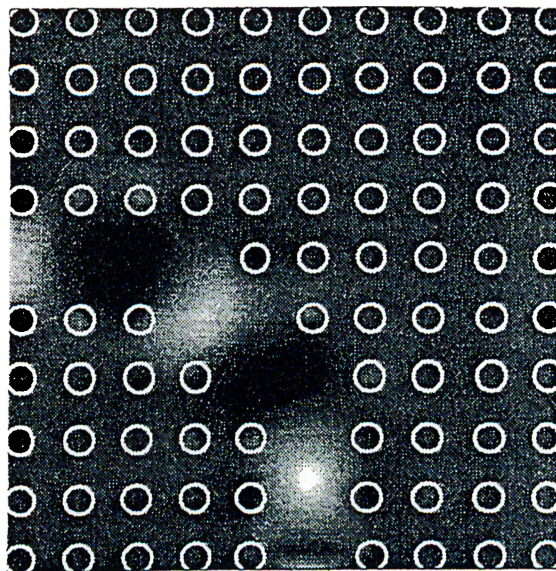


**Figure 1.6:** Theoretical simulation of a waveguide carved inside a 2-D photonic crystal.<sup>25</sup> The light is guided through defects. The bright spots correspond to enhanced optical field.

Waveguides allow only certain electromagnetic wave modes to propagate inside the structure. There are many corresponding applications, which are of great importance in technology. As metals absorb most of the power at optical frequencies, dielectric-based waveguides are usually used at optical frequencies. These structures rely on the total internal reflection of the EM waves. However, there is a problem in guiding the wave through sharp edges, and tight curves. The angle of incidence would be too high for total internal reflection when the wave turns through a tight curve. So, most of the field would be radiated and lost. To change the direction of a wave with a dielectric guide, smooth curves which require long distances are needed. On the other hand, a waveguide can be carved through a photonic crystal, in which the guided modes can travel freely (figure 1.6). Therefore the trapped wave is guided without loss through the carved waveguide, even if it has tight corners.<sup>25</sup> This would be helpful in lowering the size of integrated optical circuits.

## 1.6 Metallic photonic crystals and other applications

Although metals are quite lossy at optical frequencies, they act as perfect conductors at microwave and millimeterwave frequencies. The initial interest for metals in PBG studies arised from the idea of obtaining high attenuation with fewer number of layers compared to the dielectric-based crystals. With a very low filling ratio and few number of layers, much lighter photonic crystals can also be achieved. The experiments show that the metallic photonic crystals have stop bands starting at zero frequency up to a cut-off frequency  $v_c$ .<sup>26,27</sup> This high-pass stopband is called as the metallicity gap. At higher frequencies, due to the periodicity of the structure, other stop bands are also observed. These are the band gaps, with lower and upper band edges, as in dielectric structures. Experiments on defect structures in metallic crystals also show similar localizations of electromagnetic waves.<sup>26,27,28</sup> However, the Q-factor of those defect modes are lower than those of the dielectric photonic crystals.

Beyond these, at microwave and millimeterwave frequencies, many other possible applications may be developed. A doped photonic crystal, in which the frequency of the localized mode is tuned to the desired frequency, may act as a bandpass filter. The frequency of this mode may be sensitive to temperature, or to the length of an object placed inside the crystal. So the photonic crystal may be used as a tunable sensor for temperature, length or any other such external parameter.

## 1.7 Summary of this work

Using the layer by layer photonic crystal, we first worked on the characteristics of simple defects. Then, we worked on the reflection and transmission characteristics of dielectric-based photonic crystals. We observed that the phase of the reflected waves had strong polarization dependence. The properties of the crystals with planar defects; which are analogous to Fabry-Perot resonators, were investigated.

Using the phase information of the reflected waves from the mirrors of the defect (or cavity), a simple method to predict the defect frequency was developed.<sup>29</sup> The predicted frequencies were in good agreement with the experimental data. The theory was similar to that of Fabry-Perot resonators, where the localization of the wave occurred when phase shift in a round trip was a multiple of  $2\pi$ . The transmission spectra of the walls of the cavity was compared with the Q-factors of the defect modes. The quality factor of the defect mode was inversely proportional to the transmitted power from the walls of the cavity. High Q factors, around 5000, were observed for the defect modes within the stop band.

Metallic photonic crystals built around layer-by-layer geometries were also investigated. The reflection and resonance experiments performed with this metallic crystal gave results similar to that of the dielectric crystals. On the other hand, the attenuation per layer in a metallic structure was observed to be around 8 dB: This is much higher than the values obtained from the dielectric-based crystals, which is around 4 dB. Planar defects and defects formed by the removal of the rods were studied, both in simple tetragonal (st) and face-centered-tetragonal (fct) like layer by layer metallic structures. Transmission, reflection and defect mode comparisons of st and fct type crystals were made. Reflection characteristics of crystals with defects were investigated. Strong reflection rejections at corresponding defect frequencies were observed.

Finally, the properties of the field around a defect were studied by using a monopole antenna which was placed inside the defect as a detector. By placing a Schotky-diode detector inside the cavity, experiments were performed to understand the resonant cavity enhancement of the field. The measurements are made by a monopole antenna inserted into the defect structure. The antenna output was measured by a Schotky-diode detector. For cross check, the measurements were also performed by connecting the monopole antenna to a network analyzer, and to a powermeter respectively. It was observed that the initial field was enhanced nearly 200 times inside the resonant cavity.

# **Chapter 2**

## **Reflection Properties and Defect Formation**

Two basic properties of photonic crystals are important for the applications mentioned in the previous chapter. First, they act like ideal mirrors at their stop bands. Second, localization of EM waves is possible by the introduction of defects. To investigate these concepts, a photonic crystal is built, which is suitable for both fabrication and modification purposes. We first work on the transmission properties of the crystal, and the characteristics of various types of defect structures. Since similar work was done for many type of photonic crystals, and even for this layer-by-layer geometry previously,<sup>18,23</sup> we just give a summary of the work. Later on, we investigate the reflection properties of the crystal, and use this information to develop a simple model which explains the defect formation in photonic crystals. For the characterization of the defects, a theory analogous to the theory of the Fabry-Perot resonators is used. This analogy is successfully used to predict the frequencies and the Q-factors of our defect modes.

### **2.1 Defect structures**

The crystal used in our experiments has the dielectric layer-by-layer crystal geometry shown in figure 1.3. The square-shaped alumina rods used to construct

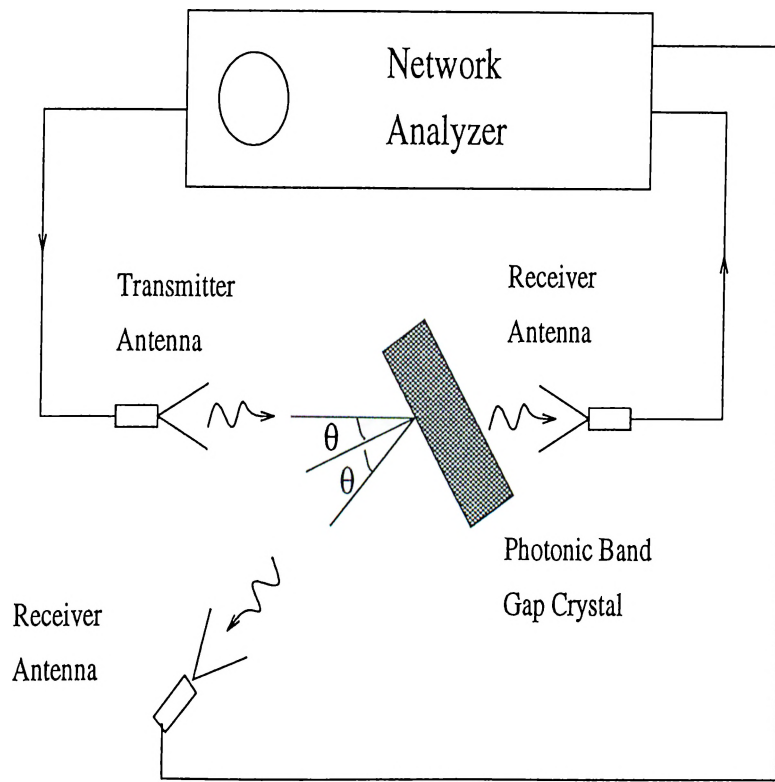


**Figure 2.1:** Experimental setup  
Experimental setup for simultaneous reflection and transmission measurements

the crystal have the dimensions of  $0.32\text{ cm} \times 0.32\text{ cm} \times 15.25\text{ cm}$ . We chose a  $1.12\text{ cm}$  center to center separation, corresponding to a filling ratio of  $\sim 0.29$ . A single unit cell is formed by 4 layers in the stacking direction. The size of the crystal is kept large, for the purposes of easy fabrication, modification and measurement. But the dimensions can easily be scaled to higher frequencies by silicon micromachining techniques. The experimental setup for the measurements is shown in figure 2.1. Using this setup, we can perform simultaneous reflection and transmission measurements for different incidence angles ( $\theta$ ) of the incoming EM waves. An HP 8510C network analyzer and three set of microwave horn antennas are used for characterization.

The transmission spectra of a 16-layer (4 unit cell) crystal is shown in figure 2.2. The crystal has a stop band between 11 and 13 GHz along various crystal directions, which are in good agreement with the theoretical calculations.<sup>31</sup> The

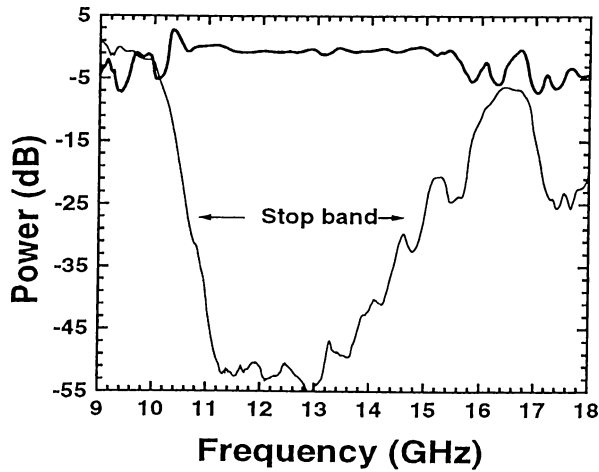


**Figure 2.2:** Reflection and transmission characteristics  
Reflection (thick solid line) and transmission (thin solid line) intensity of 4 unit cells  
(16 layers) of photonic crystal

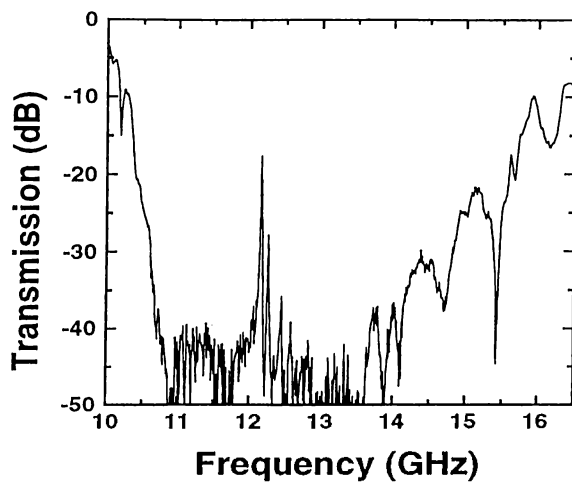


**Figure 2.3:** Transmission from a single rod removed defect structure  
Transmission spectra from a 16-layer photonic crystal, where 8<sup>th</sup> layer is chosen as the  
defect layer.

attenuation obtained from the crystal exceeds 50 dB within the stopband.

Various kinds of defect structures built around this photonic crystal are

studied. The defects under study are acceptor type of defects, where some part of dielectric material is removed from the crystal. Figure 2.3 shows the transmission spectra of a typical defect structure produced by removing a single rod from the middle of a 16 layer crystal. The transmission spectra is not different from that of the defectless crystal. We just observe a peak in the transmission at the localized mode frequency (12.16 GHz). The quality factor of the mode is 1380 and the peak transmission at maximum is -17.65 dB below the incident signal.

## 2.2 Reflection measurements

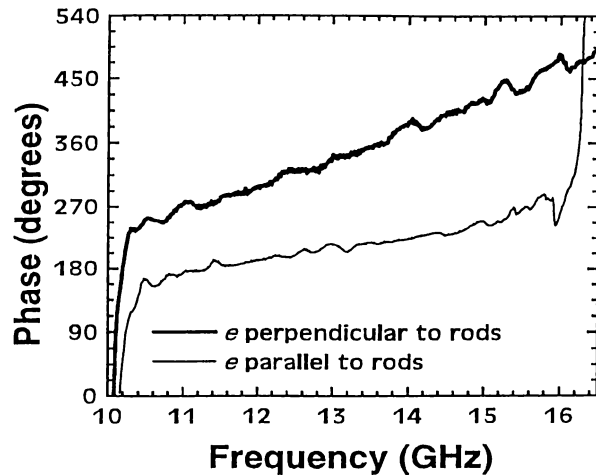


**Figure 2.4:** Phase information

The phase of reflected wave from an 8 layer crystal for two different polarization, where the polarization vector  $e$  of the incident EM wave is either perpendicular (thick solid line) or parallel (thin solid line) to the rods of the top layer of the photonic crystal.

Later on, we concentrated on reflection measurements. The calibration of reflection measurements is achieved with an Aluminum metal plate, which has 99.96% reflectivity. The simultaneously taken reflection and transmission magnitudes of a 16 layer crystal along the stacking direction with an incidence angle  $\theta = 5^\circ$  is shown in Figure 2.2. Total reflection occurs within the band gap, where the transmission

drops below -50 dB. The magnitudes of the reflected and transmitted waves were found to be independent of the polarization vector  $\mathbf{e}$  of the incident EM wave.

The reflection phase measurements are rather difficult to perform. The flatness of the top surface of the photonic crystal and the positioning of the photonic crystal with respect to the calibration metal plate are very critical for a reliable measurement. The measurements are performed within an accuracy of  $\pm 5^\circ$ . We observed a strong polarization dependence for the phase of the reflected waves. The reflection phase characteristics of a crystal made of 2 unit cells (8 layers) are shown for both polarizations in figure 2.4, where the angle of incidence is  $5^\circ$ .

## 2.3 Fabry-Perot analogy

The reflection phase information can be used to understand the defect formation in photonic crystals. The defects we investigated for this purpose are formed by separating a full 16 layer crystal from the middle. The introduced planar air gap inside the crystal produces acceptor like defect modes. Our system can be considered as an analog of a Fabry-Perot resonator, with the introduced planar defect acting as the cavity, and the 8-layer photonic crystals on each side acting as the mirrors. The localization in the cavity obtained in this way can be quite high. The transmission spectra for such a defect where the separation length is 4.6 mm is given in figure 2.5 in an expanded frequency scale. The quality factor of the peak is found to be around 5300, which is the highest value obtained up to now for such a 3-D photonic crystal structure.

At this point, we will use the reflection phase information to predict the frequency of the defect modes. The theory we will use is analogous to that of the Fabry-Perot type of resonators.<sup>32</sup> In this analogy, to find the circulating field  $E_c$  inside the crystal, we add the transmitted field through the front mirror, and the reflected component after a round trip inside the cavity:

$$E_c = j t_1 E_i + r_1 r_2 e^{-j(2\beta L + \phi_1 + \phi_2)} E_c \quad (2.1)$$

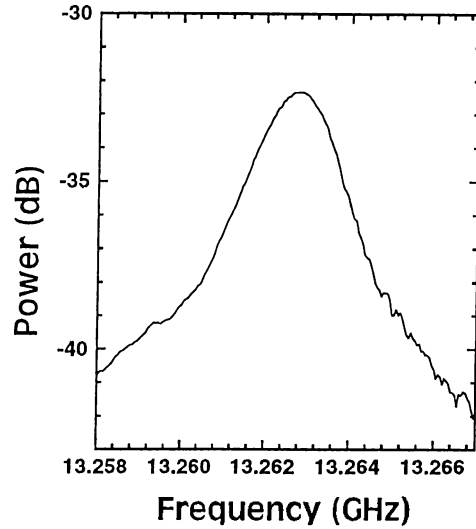


**Figure 2.5:** High Q factor defect mode.  
Expanded frequency scale for the defect mode, which has a Q factor of 5300

where  $E_i$  is the initial wave,  $t_1$  is the transmission coefficient of the front mirror,  $r_1 e^{-j\phi_1}$  and  $r_2 e^{-j\phi_2}$  are the reflection coefficients of mirrors,  $\phi_1$  and  $\phi_2$  are the reflection-phase factors in radians,  $\beta$  is the propagation constant for the travelling EM wave in air, and  $L$  the separation length of the cavity. So, the ratio of the circulating field to the initial field can be calculated as:

$$\frac{E_c}{E_i} = \frac{j t_1}{1 - r_1 r_2 e^{-j(2\beta L + \phi_1 + \phi_2)}} \quad (2.2)$$

The resonance condition is satisfied when the phase shift due to one round trip is a multiple of  $2\pi$ , that is when  $2\beta L + \phi_1 + \phi_2 = 2m\pi$  ( $m = 0, \pm 1, \pm 2, \dots$ ). This resonance condition with the obtained reflection-phase information, can now be used to predict the frequency of the defect mode.

Changing the separation length  $L$  of the resonator, we obtained the transmission properties and the frequencies of the defect mode. The defect modes, first appearing at the upper band edge, shifts to the lower band edge of the stop band, as the separation length  $L$  is increased. If the separation is further increased to 10.0 mm., we start to observe secondary defects appearing at the upper band edge. In the mean time, the first defect shifts further down

Separation width L (mm)	Frequency GHz		$\phi_t(f_L)$ (degrees)	
	m=1	m=1	m=2	m=2
3	13.97	260		
4	13.50	230		
5	13.13	202		
6	12.54	170		
7	12.15	156		
8	11.78	134		
9	11.45	113		
10	11.16	92	15.34	352
11	10.86	73	15.01	324
12	10.66	53	14.66	298
13	10.45	34	14.31	274
14			13.98	250

**Table 2.1:** Experimental measured defect frequencies and corresponding total phase contributions from the walls of the cavity for resonance condition are given for different separation widths, for the first ( $m=1$ ) and second ( $m=2$ ) defect modes.

to lower frequencies to disappear at the lower band edge. To make a comparison of the theory with the experiment, we added the reflected phase measured from the two walls of the cavity  $\phi_{t,ex} = \phi_1 + \phi_2$ . Then, we compared it with the phase that should correspond to the defect frequency in the resonance condition which is given as,

$$\phi_t(f_L) = 2m\pi - 4\pi L \frac{f_L}{c} \quad (m = 0, \pm 1, \pm 2, \pm 3, \dots) \quad (2.3)$$

where  $f_L$  is the defect frequency corresponding to the separation width  $L$ . Table 2.1 lists the measured frequencies of the defect modes, the value of  $m$  and the calculated  $\phi_t(f_L)$  as a function of separation length  $L$ . In figure 2.6, the predicted  $\phi_t(f_L)$  and the measured  $\phi_{t,ex}(f)$  total phase of the two mirrors are compared. As can be seen from the plot, the predicted phase values are in very good agreement with the measured phase values.

Using this reflection-phase information, the frequency of a defect mode for

any given separation width  $L$  can be found by solving the following equation by an iteration method.

$$f_L = \frac{c}{4\pi L} [2m\pi - \phi_{t,ex}(f_L)] \quad (2.4)$$

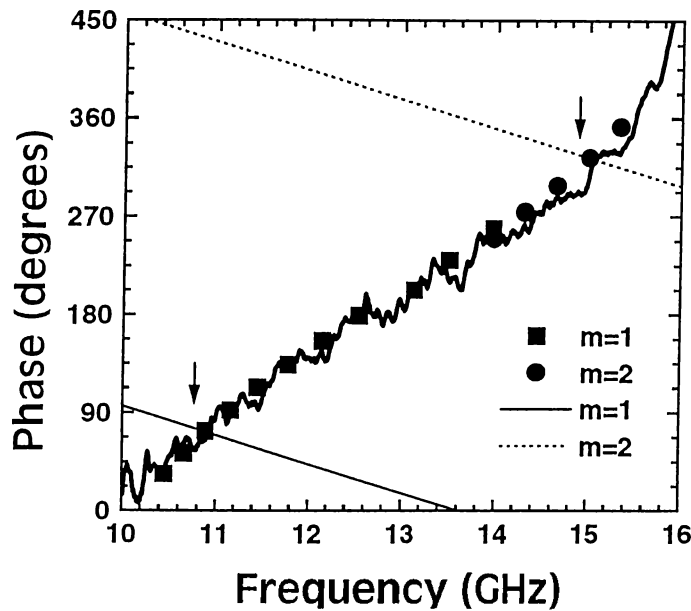


**Figure 2.6:** Phase comparison

Comparison of experimental total reflection-phase contribution (thick solid line) of the walls of the cavity, with the calculated values for  $m=1$  (squares) and  $m=2$  (circles) for different separation widths. The plot of  $\phi_t(f)$  for  $m=1$  (thin solid line) and  $m=2$  (dotted line) are also shown for  $L=11$  mm.

The defect frequency  $f_L$  can also be predicted by graphical methods. The total phase of the two mirrors  $\phi_{t,ex}(f)$  is plotted along with  $\phi_t(f) = 2m\pi - 4\pi L \frac{f}{c}$  as a function of  $f$ . The defect frequency  $f_L$  for the chosen length  $L$  can be found from the intersection points of these two plots. As an example, the defect frequency predicted for  $L=11$  mm, is shown in figure 2.6. The plot of  $\phi_t(f)$  is made for  $m=1$  (thin solid line) and  $m=2$  (dotted line), and these two lines intersect with the  $\phi_{t,ex}(f)$  at two frequencies (indicated by arrows in the figure), which are

both within the band gap. We see that the agreement between the predicted and experimental defect frequencies is very good. This graphical method also explains the double defect formation for certain cavity lengths. If one of the defect frequencies is closer to the lower band edge, say corresponding to  $m=1$  mode, a second frequency satisfying the resonance condition for  $m=2$  can be found. An example where double defects are observed for  $L=11.5$  mm, is given in figure 2.7. The  $m=1$  defect mode corresponds to 10.76 GHz, while  $m=2$  mode corresponds to 14.84 GHz. As the separation is further increased, modes corresponding to  $m=3,4,5,\dots$  may also be observed.

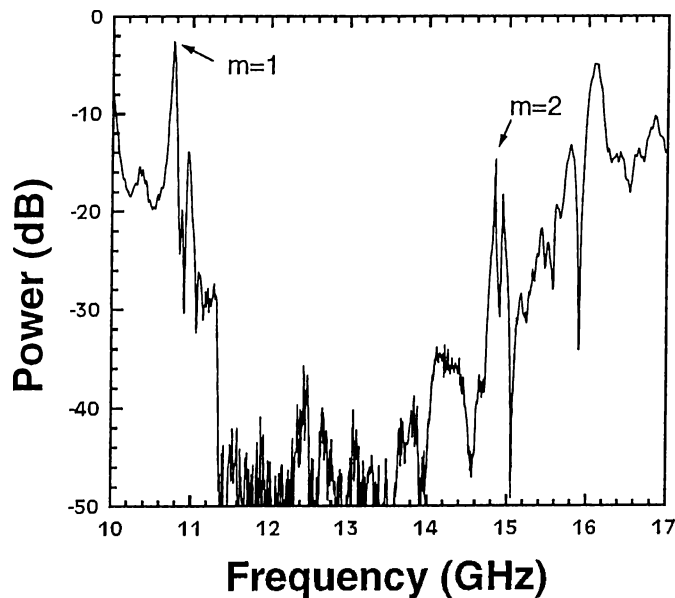


**Figure 2.7:** Double defect

An example for double defect formation, where the resonance condition is satisfied for two separate frequencies.

Although small in size, there are extra defect modes that does not seem to fit to this theory for any value of  $m$ . These extra modes may be due to the oscillatory nature of the  $\phi_{t,ex}(f)$ , so that the resonance condition is satisfied at more than one frequency for a single mode, say  $m=1$ . In other words, graphically,

there are more than one point that the expectation line  $\phi_t(f)$  cuts the  $\phi_{t,ex}(f)$  for a given  $m$  value. Another reason for multimode formation can be the occurrence of secondary resonances, or splittings. This may happen due to the misalignment of the mirrors with respect to each other, and due to the surface roughness of the photonic crystals. These effects may explain the situation, but later experiments done by metallic structures brought some different explanations, which would be discussed in chapter 3.

## 2.4 Quality Factor

A simple approach to relate the quality factors of the defect modes to the reflectivities of the mirrors can be derived by using the Fabry-Perot resonator analogy. If we calculate the square of the field, which is proportional to power:

$$\begin{aligned} E_c \cdot (E_c^*) &= \left| \frac{jE_i t_1}{1 - r_1 r_2 e^{-j2\theta}} \right|^2 \\ &= \frac{E_i^2 t_1^2}{(1 - r_1 r_2)^2 + 4r_1 r_2 \sin^2 \theta} \end{aligned} \quad (2.5)$$

where  $\theta = \beta L + \frac{\phi_t(f)}{2}$ . The magnitude of the field drops to its half value at

$$\sin^2 \theta_{1/2} = \frac{(1 - r_1 r_2)^2}{4r_1 r_2}$$

When the resonance condition is satisfied,  $\theta$  will be close to  $q\pi$  radians, that is  $\theta \simeq q\pi + \theta_{1/2}$ . So full width at half maximum for  $\theta$  can be written as

$$2\theta_{1/2} = \Delta\theta_{1/2} = \frac{1 - r_1 r_2}{\sqrt{r_1 r_2}} \quad (2.6)$$

This is the condition where the peak drops to its half value. The sharpness of the peak is defined with the quality factor ( $Q$ ) of that peak, which is the ratio of the frequency of the defect to the full width at half maximum:

$$Q = \frac{f}{\Delta f_{1/2}} \quad (2.7)$$

Assuming linear dependence of  $\phi_t(f)$  on  $f$  with a constant  $\alpha$ , that is letting

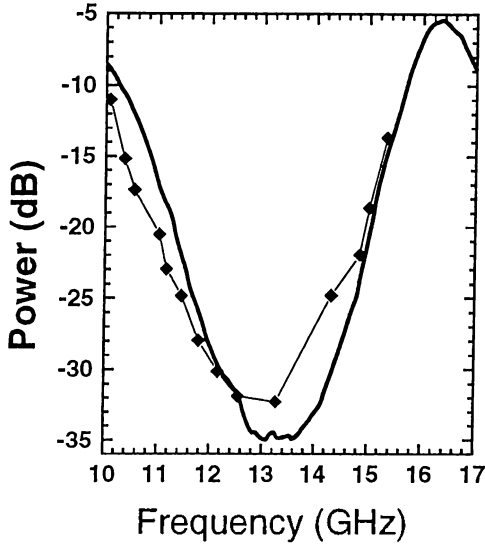


**Figure 2.8:** Inverse Q factor and Transmission

The comparison of inverse of Q values (diamonds) with the corresponding 8 layer transmission (thick solid line).

$\phi_t(f) = \alpha f$  within the band gap, we can relate  $\Delta\theta_{1/2}$  to  $\Delta f_{1/2}$  as:

$$\Delta f_{1/2} = \left( \frac{2\pi d}{c} + \frac{\alpha}{2} \right)^{-1} \Delta\theta_{1/2} \quad (2.8)$$

and with this formalism, f can be written from the resonance condition as:

$$f = m\pi \left( \frac{2\pi d}{c} + \frac{\alpha}{2} \right)^{-1} \quad (2.9)$$

So the quality factor Q value can be calculated from the equation 2.7 as:

$$Q = \frac{m\pi}{\Delta\theta_{1/2}} = m\pi \frac{\sqrt[4]{R_1 R_2}}{1 - \sqrt{R_1 R_2}} \quad (2.10)$$

where we defined the reflectivities of the mirrors as  $R_1 = r_1^2$  and  $R_2 = r_2^2$ . In our case, where  $R_1 = R_2 = R$ , and the transmittances  $T_1 = T_2 = T = 1 - R$  are all equal, we may simplify the Q value to:

$$Q = m\pi \frac{\sqrt{R}}{1 - R} = \frac{m\pi}{T} \quad (2.11)$$

with the assumption that reflectance  $R$  is nearly unity inside the stop band. Using this information, a comparison of the  $Q$  value, with the transmittance obtained from one wall of the cavity (which is 8 layers), is made. The plot in figure 2.8 shows the transmittance of 8 layers, and  $\frac{m\pi}{Q}$  as a function of frequency of the corresponding defect. As can be seen from the graph, the general trend of the plots are similar, however, the experiment does not quite fit to theory quantitatively. The reason may be due to the finite size of the crystal. As we are not using very long rods, the field may not be as localized as the theory presumes, resulting in lower  $Q$  values. (2.11)

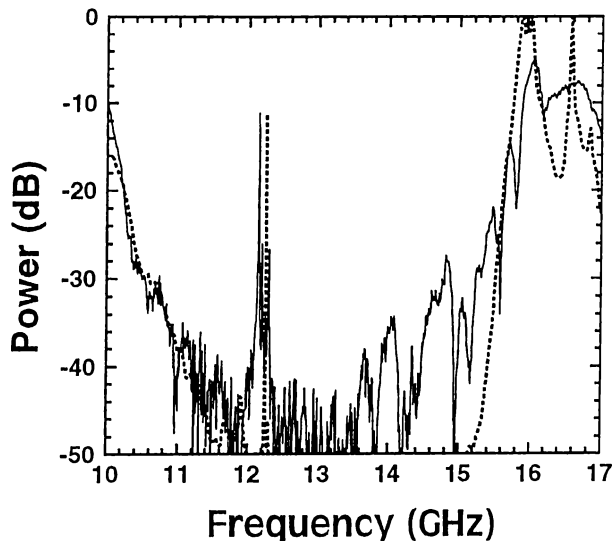


**Figure 2.9:** Comparison of defect theory with experiment  
The comparison of calculated (dashed line) and experimental (solid line) transmission characteristics of a Fabry-Perot cavity with a 7 mm separation.

Going one step further, we tried to simulate the transmission spectra of the crystal with defect. The ratio of transmitted field through the resonator to the

incident field can be calculated as:

$$t = \frac{E_t}{E_i} = \frac{Te^{-j\beta L}}{1 - Re^{-(2j\beta L + \phi_t)}} \quad (2.12)$$

We inserted the experimental values of 8 layer transmittance  $T$ , reflectance  $1 - T$  (since  $R$  is so close to 1, we preferred to use  $1 - T$  instead of  $R$ , which is more experimentally significant), and  $\phi_t$  the total phase contribution from the two walls of the cavity into equation 2.12. Then, we calculated the transmitted power, in dB units, for a range of frequencies for certain chosen separation widths as:

$$\text{Power}(dB) = 10 \log(|t|^2) \quad (2.13)$$

The comparison of this theory with the experimental transmitted power is given in figure 2.9, for a structure where separation width of the cavity is  $L=7$  mm. Some amount of the circulating field is lost in each round trip due to the finite size of the crystal. Because of this, a relative small loss coefficient is also added to the equation to simulate the reality. As we are limited by the noise level of our experimental setup, we can not obtain as high attenuation as the model presumes inside the band gap. However, the frequency and the peak amplitude of the defect mode presumed by the model quite agree with the experimental results. We also see that the band edges are also located around the same frequencies.

# **Chapter 3**

## **Metallic Photonic Crystals**

Photonic crystals have wide variety of applications at microwave and millimeter wave frequencies, as mentioned in chapter one. Many type of dielectric-based photonic crystals (DPC) were proved to be successful for these applications. However, some problems still exist for these crystals. The rejection ratio of a DPC is typically limited to a maximum of 3-4 dB per layer,<sup>33</sup> which requires a significant number of layers for isolation purposes. Besides, for lower frequency applications around 1-10 GHz, corresponding dielectric crystals are very large and unpractical, with a typical size at the order of one square meter. A typical alternative to DPC are metallic based crystals (MPC), which solve these problems. Although metals exhibit high absorption at optical frequencies, they act as perfect conductors at microwave and millimeter-wave frequencies, minimizing the problems related to absorption.

### **3.1 Structure**

The experimental set up used for characterization is similar to the one described in chapter 2 (see figure 2.1), where we used metallic crystals instead of dielectric crystals. We have three set of horns, which we can use to scan the measurement frequency from 8 GHz up to 26 GHz. The metallic crystal we investigated is a layer-by-layer structure formed by square shaped aluminum plates. Each plate

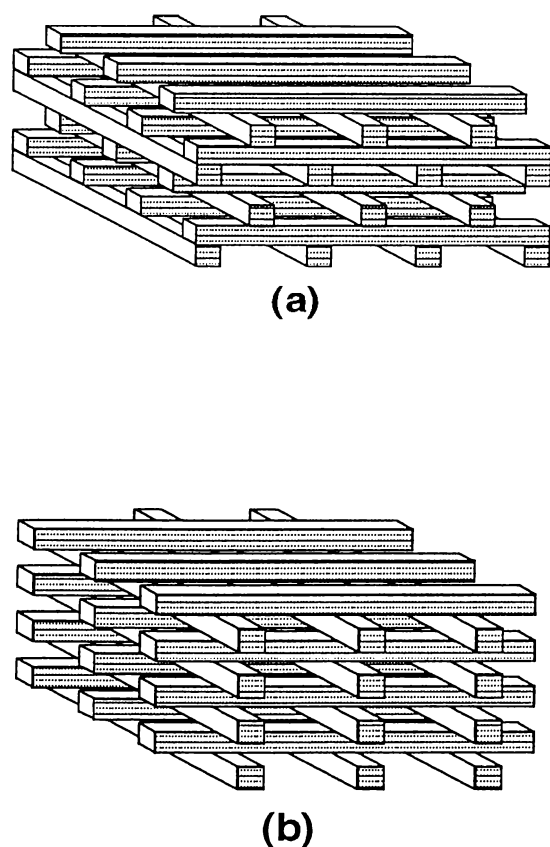


**Figure 3.1:** Two types of layer-by-layer photonic crystals  
(a) Face-centered tetragonal (fct), and (b) simple tetragonal (st) type photonic crystals.

is carved from bottom and top, so that one plate have two layers of the crystal. Top layer has a number of parallel rods, which are perpendicular to the rods of the bottom layer. Two different types of crystals are formed by stacking these plates in two different forms. By shifting every second plate half a unit cell, in

the diagonal direction of the plates, with respect to the first one, a face-centered-tetragonal (fct) structure is obtained, as shown in figure 3.1(a). The structure is similar to the dielectric crystal used in chapter 2. The second type of crystal is a simple tetragonal (st) structure, shown in figure 3.1(b). The plates are brought together without any shift, so that one single plate, that is two layers, is a unit cell in the stacking direction. We worked on the properties of both type of crystals. The rods were 0.8 mm thick, 2.5 mm wide, and 120 mm long. The center to center separation between adjacent parallel rods was 7.6 mm. Each plate, which is formed of two layers of crystal, has the dimensions of 150x150x5 mm.

## 3.2 Transmission properties

We first investigated the transmission characteristics of the crystals. Figure 3.2 shows the transmission spectra of st (a) and fct (b) structures as the number of layers are increased. As expected from a metallic crystal, we have an upper edge of the band gap, while there is no lower band edge. That is, the band gap extends from zero frequency to a cut off frequency  $\nu_c = 20$  GHz, which is called “metallicity gap”. This cut-off frequency may be predicted as the half of the frequency of the spatial frequency corresponding to the periodicity of the crystal. The attenuation per layer is about 7-8 dB, which is quite high when compared to 3-4 dB attenuation per layer of a dielectric-based photonic crystal.

For the calculations of the EM wave transmission through the photonic crystals, the transfer matrix method (TMM) introduced by Pendry and MacKinnon,<sup>34</sup> is used. In TMM, the total volume of the photonic crystal is divided into small cells. The fields in each cell are coupled with those in the neighboring cells. Then the transfer matrix can be defined by relating the incident fields on one side of the photonic crystal with the outgoing fields on the other side. Using TMM, the band structure of an infinite periodic system can be calculated. But the main advantage of TMM is for the calculation of transmission and reflection coefficients for EM waves of various frequencies incident on a finite thickness slab of the photonic crystal. In that case, the material is assumed to be

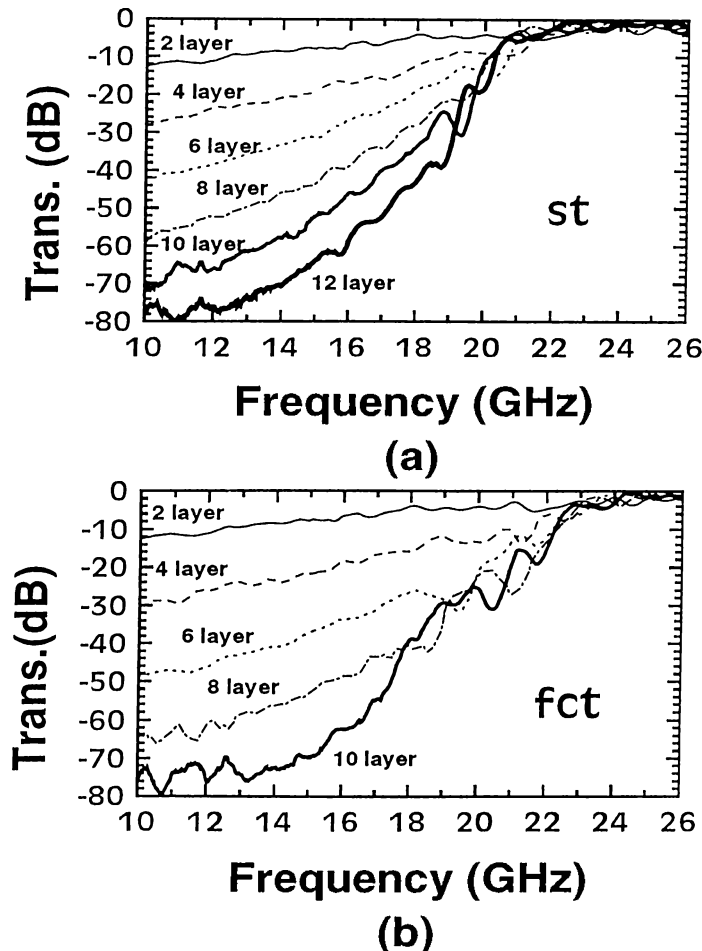


**Figure 3.2:** The transmission characteristics of fct and st metallic structures  
 (a) Transmission of st type of crystal, as the number of layers are increased from 2 layers (thin solid line) up to 12 layers (thick solid line). (b) Transmission of fct type of crystal, as the number of layers are increased from 2 layers (thin solid line) up to 10 layers (thick solid line).

periodic in the directions parallel to the interfaces. The TMM has previously been applied in studies of defects of dielectric-based layer-by-layer PBG materials,<sup>23</sup> of photonic crystals in which the dielectric constants are complex and frequency dependent,<sup>35</sup> and in metallic photonic crystals.<sup>26</sup> In all these examples, the agreement between theoretical predictions and experimental measurements were very good.

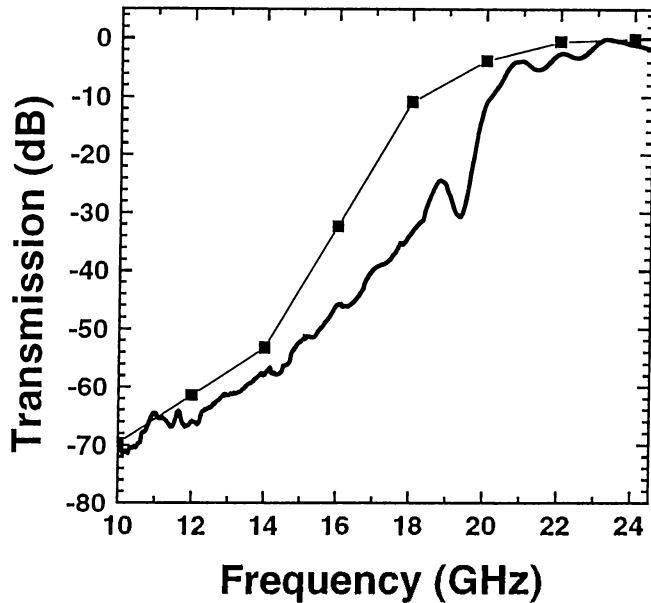


**Figure 3.3:** Transmission from 10-layer metallic photonic crystal  
Comparison of the experimental transmission (thick solid line) of the 10-layer metallic crystal with the theoretical simulations (thin solid line).

The experimental transmission characteristics of a ten layer crystal is compared, with the computer simulations performed by M. Sigalas and K.M. Ho of ISU, in figure 3.3. We see that the simulation, in which TMM is used, agrees well with the experiment. The band edge is located around same frequency of 20 GHz. The attenuation obtained inside the gap is around 70 dB for both results. In the computer simulations, TMM is used, where each unit cell is divided into 12x12x8 cells. Although the conductivity of the metal is very high, because of convergence problems of TMM, a smaller value is chosen for the simulations. The small discrepancy between the model and the experiment may arise from this approach.

For the fct crystal, we also checked the dependence of the transmittance on incidence angle  $\theta$  of the incoming wave. The results of transmittance with increasing  $\theta$  is seen in figure 3.4. As the angle is increased, we see a shift in the

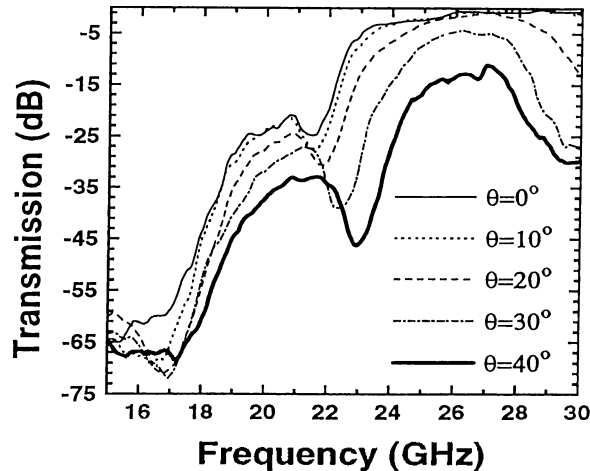


**Figure 3.4:** Transmission at different angle of incidences.

Transmission properties of 16 layer fcc metallic photonic crystal as the angle of incidence changes from 0 (thin solid line) to 40 degrees (thick solid line).

cut-off frequency of the band. This shift is expected, since the periodicity length of the crystal sensed by the travelling wave is lowered with the increasing angle. We also see a secondary gap arises at a slightly higher frequency, due to the periodicity of the crystal. This is a band gap similar to the ones in the dielectric crystals, where we have both the low and high band edges, enabling us to call this gap a photonic band gap. However it is not obvious if this gap is persistent for all directions. We also see the signs of a higher frequency band appear around 30 GHz, but this is hard to explore since we are at the frequency limits of our experimental setup.

### 3.3 Defect structures

Similar to dielectric-based crystals, defect structures formed around metallic crystals result in localization of EM waves.<sup>26,27,28</sup> The defects are created by removing a single rod from the middle of the crystal. The transmission for fcc and st crystals, both with thicknesses of 14 layers, and both with the same defect

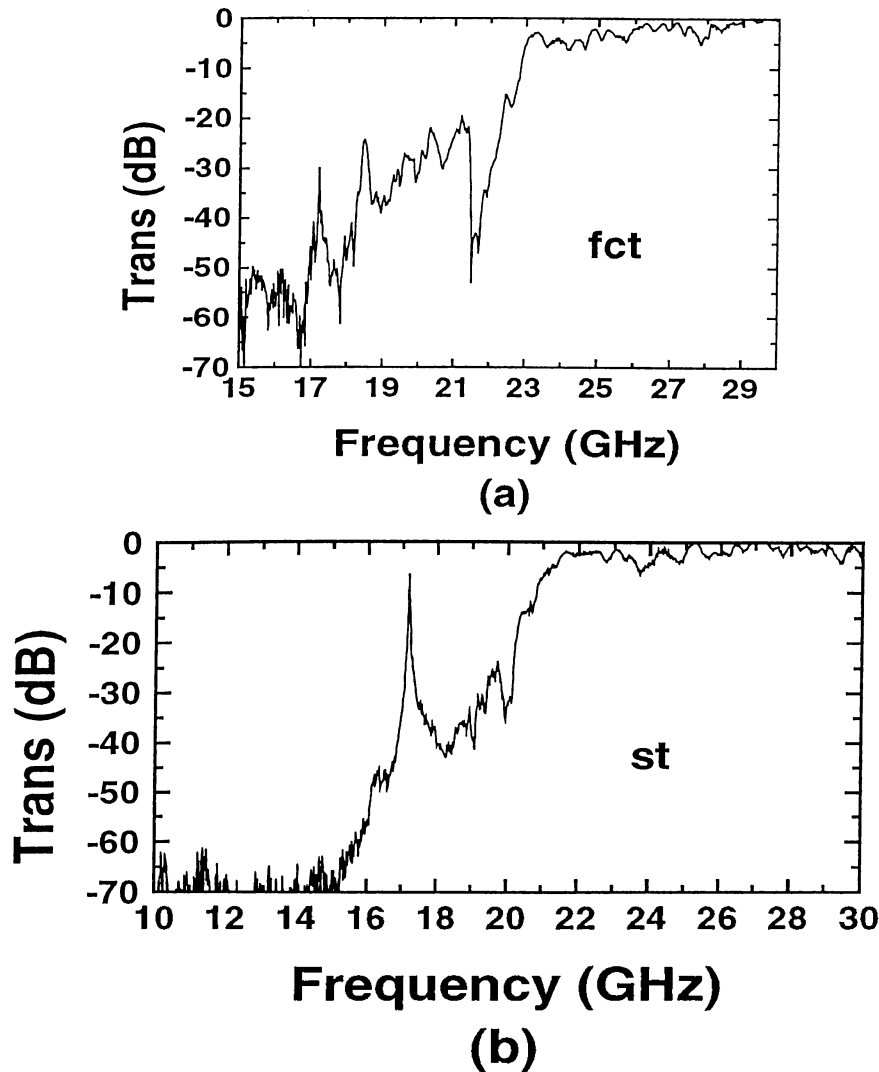


**Figure 3.5:** Comparison of the transmission characteristics of defect structures of st and fct crystals.

(a) Transmission of an fct 14-layer defect. (b) Transmission of an st 14-layer with the same defect.

structure, are compared in figure 3.5. The quality factor of the fct type structure is around 950, higher than that of the st structure, which is around 700. This can be explained by the higher attenuation per layer property of an fct crystal (compared to st crystal). However, the maximum transmission of the peak is 20

Defect Type	Number of Layers	Peak Freq. (GHz)	Peak Max. (dB)	Q
single rod rem	10	17.342	-0.001	173
single rod rem	12	17.266	-6.02	253
single rod rem	14	17.175	-6.37	746
single rod rem	16	17.277	-14.25	1212
single rod rem	18	17.19	-19.06	1637
periodic rod rem	10	17.21	-0.46	126
periodic rod rem	12	17.089	-7.06	201
periodic rod rem	14	17.178	-7.85	613
periodic rod rem	16	17.093	-15.75	1085
periodic rod rem	18	17.092	-23.5	1367

**Table 3.1:** The comparison of the properties of two types of defect modes for st crystal.

dB less than the incident signal for the fct crystal, which puts a limit to achieve a higher quality factor by increasing the number of layers. If we increase the number of layers further, the maximum transmission of the peak goes down to noise level, where the signal becomes undetectable. On the other hand, the st structure for the same defect is just 6 dB less than the incident signal, which allows an increase in the number of layers to obtain higher Q-factors. Figure 3.6 shows the characteristics of an 18 layer st structure, where the 9<sup>th</sup> layer is chosen as the defect layer. This defect mode exhibited a peak transmission of -19 dB, along with a Q-factor of 1637. So, st metallic defect structures have higher peak amplitudes, and higher achievable Q-factors, when compared with fct type metallic defect structures.

We also studied the defects where every other rod from a single layer is removed, from an st type of crystal. Table 3.1 summarizes the results for the two different defect structures, as the number of layers are increased. The frequency of the defect mode is nearly constant, while the transmission maximum of the peak gets lower as the number of layers is increased. The Q-factor of a defect mode is proportional to the inverse of the transmission of the crystal on both sides of the defect, as derived in chapter 2 for a Fabry-Perot type of cavity. Similarly,

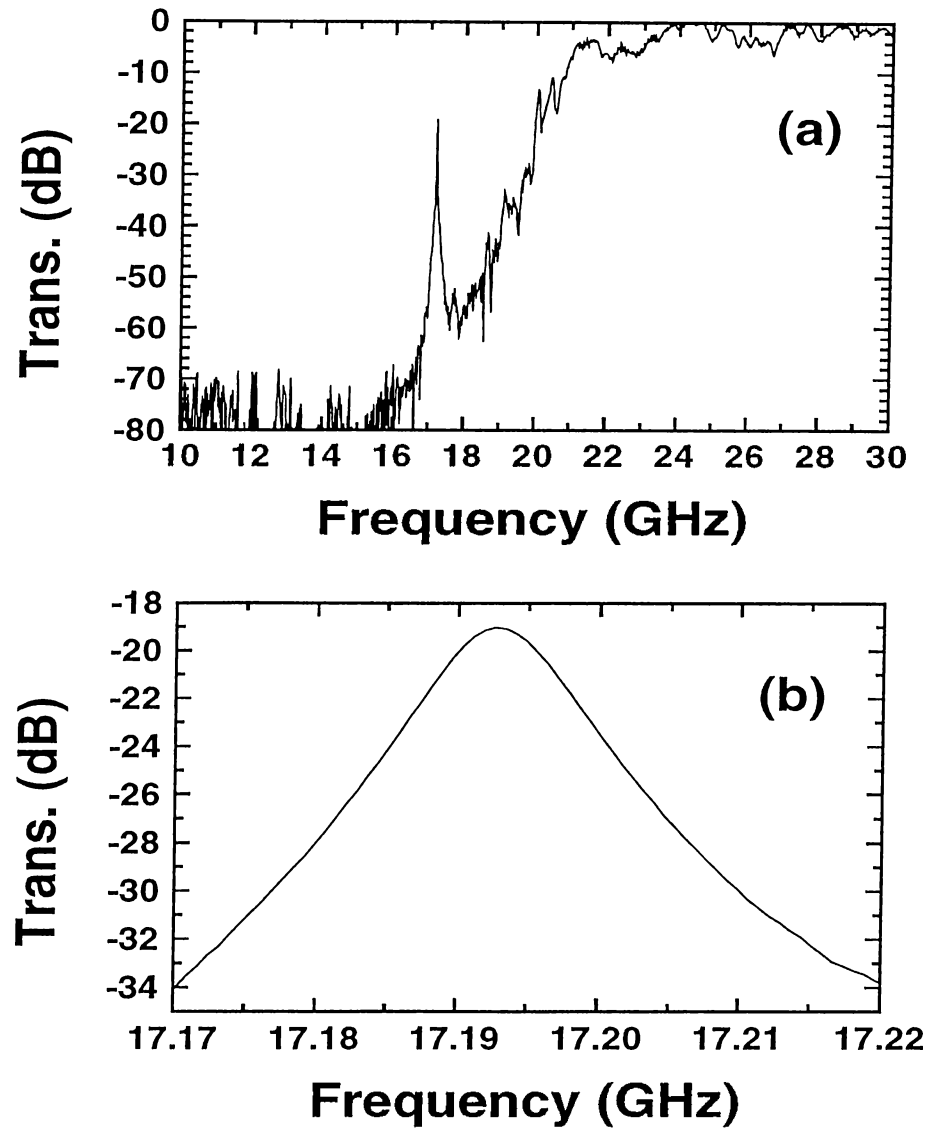


**Figure 3.6:** Transmission Characteristics of an st 18-Layer Defect.  
 (a) Transmission spectra for the defect structure generated by removing a single rod from the 9<sup>th</sup> layer of the crystal. (b) Expanded frequency scale for the defect mode.

we see a relative increase in Q value as the layer number is increased.

The TMM requires periodicity in the directions parallel to the interfaces. For comparison, we formed a planar defect by removing all the rods in a single layer. A 10-layer thick st structure where the 5<sup>th</sup> layer is chosen as the defect

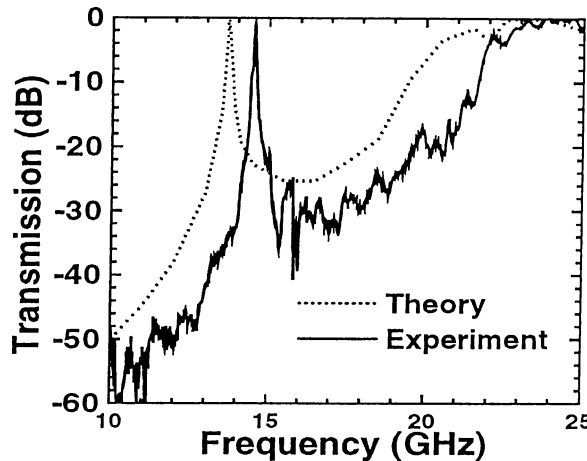


**Figure 3.7:** Comparison of Theoretical and Experimental results of a Defect Mode

Comparison of the experimental transmission properties (solid line) of the metallic planar defect structure with the TMM simulations (dashed line).

layer, is used for both theoretical simulations and experimental measurements. Calculations are again performed by M. Sigalas and K.M. Ho of ISU. Figure 3.7 compares the predicted theoretical transmission with the experimental results. As can be seen from the plot, theory and experiment are in good agreement. The peak transmission of the experiment is 0.9 dB below the incident signal, with a quality factor of 250, while the transmission of the simulation is 0.2 dB less than the incidence signal, with the same Q value of 250. However, the calculated defect frequency (13.7 GHz.) is slightly lower than the experimental result (14.5 GHz.). The discrepancy is due to the limitations coming from simulating the real structure by a discrete computer model. In present calculations, the unit cell is divided into 16x16x10 cells. By increasing the number of cells, the model gets closer to the real structure. However, the memory and computer time requirements for higher number of cells make those calculations almost impossible.

Later on, we looked for defects with high Q-factors. We know that to achieve high Q values, one has to choose defects localized at frequencies where the

rejection ratio of the crystal to the incident signal is very high. For the metallic structures, this corresponds to lower frequencies of the metallicity gap. We also know that we can easily adjust the frequency of the defect mode, for a Fabry-Perot type of cavity, using the theory presented in chapter 2. We separated a 12 layer tetragonal type of crystal from the middle. With a 10 mm separation width, a defect mode at 10.61 GHz is obtained. The Q-factor of the defect is 2250, which is quite high for a metallic structure. As expected, this results in reduced peak transmittance of the defect mode, 25 dB lower than the incident signal. Figure 3.8 shows the characteristics of this defect on an expanded frequency scale.

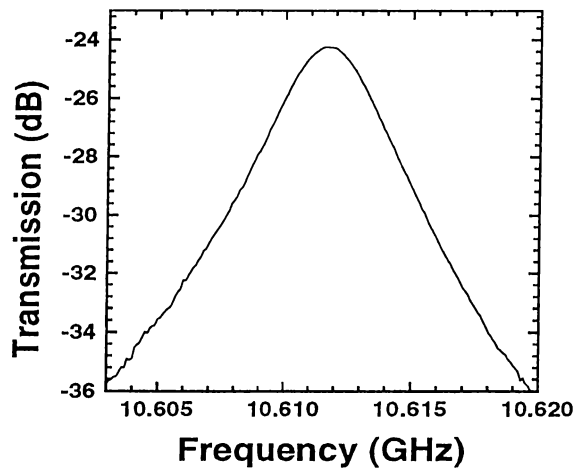


**Figure 3.8:** Defect mode with a high Q-factor.

Transmission characteristics of the defect mode with a Q-factor of 2250, in an expanded frequency scale.

We continued to explore the properties of the defects in metallic structures by changing the angle of incidence of the signal, which is achieved by rotating the crystal as described in figure 2.1. The defect structure under investigation is formed by removing a single rod from the middle of a 16 layer crystal. No significant change in the frequency or in the Q value of the defect mode is observed, when the crystal is rotated. The effective path ( $L_{eff}$ ) of the travelling EM wave in the crystal gets longer as we increase the angle of incidence. This also

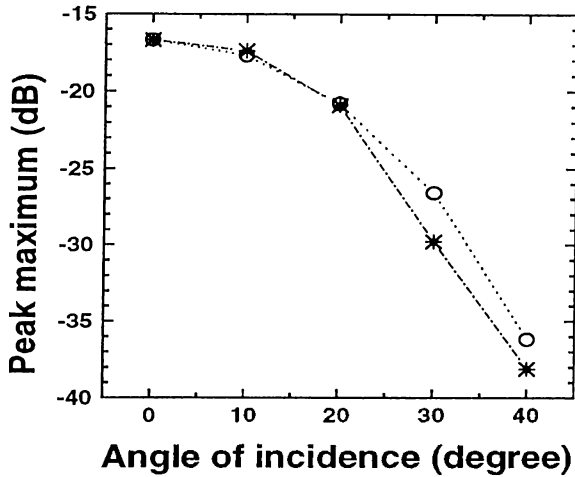


**Figure 3.9:** Comparison of experimental peak amplitudes of defect modes with the theory.

The experimentally observed peak transmissions of the defect mode as the angle of incidence is increased (stars), compared with the theoretical values (circles).

decreases the peak transmission of the defect mode obtained at increased angles of incidence. We simulated this effect by a simple formalism. Let  $L_0$  be the effective length for angle of incidence  $\theta_0 = 0$ . The decrease in the peak transmission of the defect mode is proportional to effective length  $L_{eff} = L_0 / \cos \theta$ . The attenuation for  $n$  layers of crystal,  $A(n)$ , is directly proportional to the crystal length  $L_0$ , along the stacking direction. So the drop of the peak transmission of the defect mode, when the crystal is rotated  $\theta$  degrees, is just  $A(n)/\cos\theta$ . Since the attenuation is proportional to the thickness of the crystal,  $A(n)$  can be approximated as  $A(n) = An$ , where  $A$  is the attenuation per layer obtained from figure 3.2. Then, the maximum transmittance of the defect mode at angle  $\theta$  is given as

$$Peak_{max}(\theta) = Peak_{max}(\theta_0) - \frac{A}{\cos(\theta)}n \quad (3.1)$$

where  $Peak_{max}(\theta_0)$  is the peak transmission of the defect mode at  $\theta = 0$ . The amplitudes in the above equation are in dB units. The reason behind using this logarithmic unit is simple. Since the transmission coefficients are multiplicative, the amplitudes we are dealing quickly drops to very small values. As an example,

it is very hard to notice the difference between the values of -40 dB and -50 dB in a linear plot, which correspond to 1 part in  $10^4$  and  $10^5$ , where values of the order of 1 coexists. And with this logarithmic scale, attenuation of  $n$  layers, as an example, is not  $A^n$  as in linear case, but  $nA$ , which is more significant. Experimental maximum of the peaks at given angles are compared with the results of this simple theory in figure 3.9. The agreement between the experiment and the theory is good, especially for the peak amplitudes which are higher than -25 dB. For lower amplitudes, we deviate from the theory, because of the finite dimensions of our crystal, and the noise limit of our setup.

A similar study in the Fabry-Perot cavity like defect structures gave surprising results. Increasing the angle of incidence, peaks other than the main peak at  $\theta = 0^\circ$  comes into view. If we continue to increase the angle further, we observe that a number of peaks appearing at higher frequencies dominate, while the transmission amplitude of the peaks at lower frequencies gets smaller, disappearing at noise level. The frequencies of the peaks do not shift with angle, rather, we can say they dominate at certain frequencies for certain angles. In figure 3.10, we see how new peaks emerge, and the initial peak and the lower frequency peaks vanish as the angle is increased, for a cavity length of 5 mm. It is not possible to explain these defects by the theory of double defect formation described in chapter two, since the secondary defect should be located at a much higher frequency. These double defect modes will be shown later on in this chapter. But simply, the next mode is nearly 7-8 GHz away from the first mode, while here, the frequency difference between consecutive peaks is only less than 1 GHz. One can count up to 10 peaks that dominate at different angles within the band gap. An approach can be made using the theory of resonant cavities, where the reflecting mirrors are assumed to be curved. The solution for this structure is a combination of Hermit Polynomials, which causes additional peaks to appear. But, it is still questionable why one or the other polynomial becomes dominant at higher angle of incidence. Also lens-like behavior of photonic crystals has to be shown for such an approach.

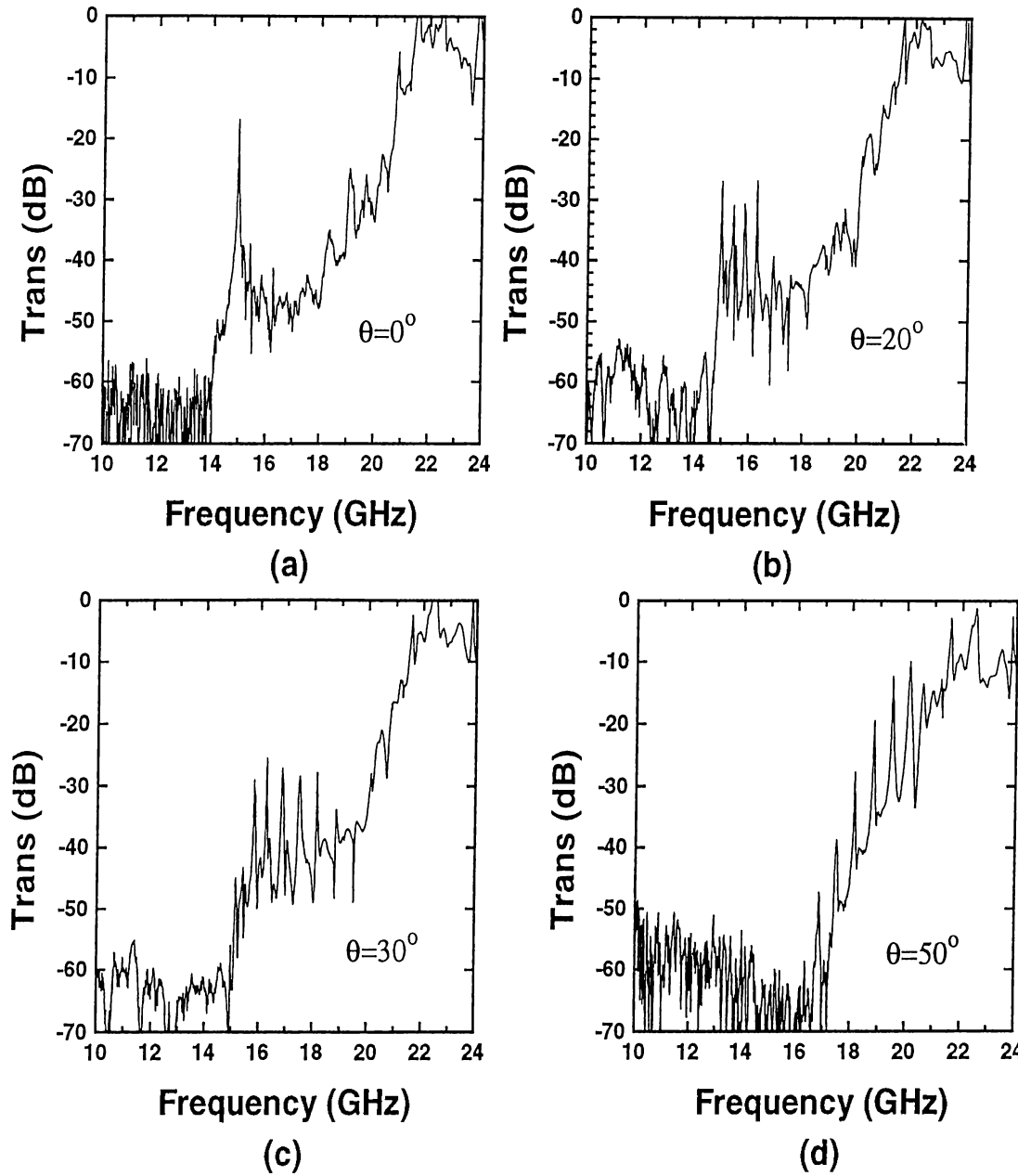


**Figure 3.10:** The additional peaks observed for the planar defect structure. The transmission characteristics of an st 12-layer planar defect structure with increasing angle of incidence.

### 3.4 Reflection properties and Fabry-Perot type cavities in metallic structures

The simultaneously taken reflection and transmission data for a 6-layer st type of crystal is shown in figure 3.11. We see the field is fully reflected within the band gap. We also see another strong reflection-band at frequencies around 25 GHz. The drop at the transmission is negligible for this band, which does not seem to agree with the reflection measurement. There may be increased absorption, or the field may be scattered at these frequencies, which minimizes the measured reflection.

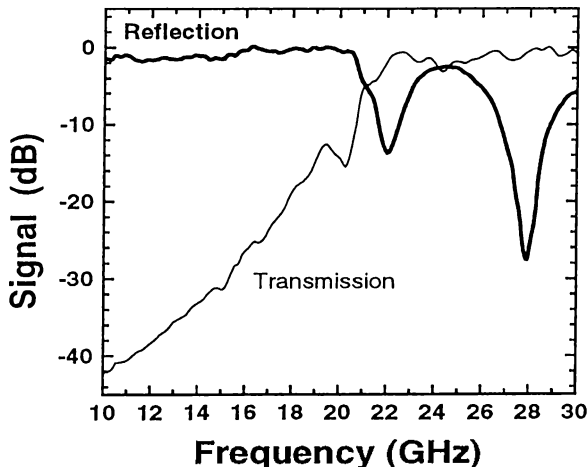


**Figure 3.11:** Reflection and transmission characteristics of st crystal  
Reflection (thick solid line) and transmission (thin solid line) characteristics of a 6-layer st crystal, where the angle of incidence is 10 degrees.

We then checked the reflection-phase properties of the metallic crystals for the investigation of Fabry-Perot type of cavities. The reflection-phase measurements are performed similar to those measurements of chapter 2, within the same accuracy. For the st structure, the reflection phase information is shown for two different polarizations in figure 3.12. The polarization mentioned here is the  $\mathbf{e}$  vector of the EM wave being either parallel or perpendicular to the front rods

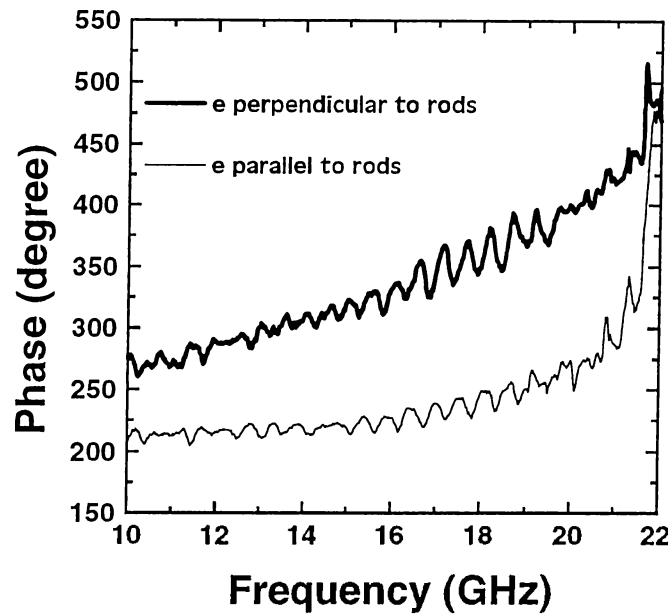


**Figure 3.12:** The reflection-phase information.

The phase of the reflected waves from the surface of the photonic crystal for different polarizations.

of the crystal. The phase slowly changes within the band gap, and the dispersion is different for different polarizations. Compared with dielectric reflection-phase information shown in figure 2.4, this crystal has much smaller dispersion for both polarizations. This reflection-phase information is used to predict the frequency of the defect mode of Fabry-Perot type of cavity, as done in chapter 2. For different separation widths of the cavity, corresponding reflection-phase contributions from the mirrors of the cavity for resonance condition at those defect frequencies are calculated. These values are then compared with the experimentally measured reflection-phase of the walls of the cavity, for two different cases.

In the first case, the cavity is formed by separating the bulk crystal of 12 layers from the middle, 6 by 6. So the surface rods on either side of the cavity are perpendicular to each other. Therefore, the total phase in figure 3.13 is obtained by adding the reflection-phases of the two walls for different polarizations.

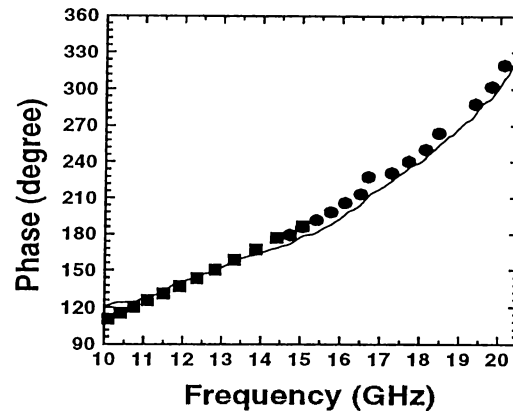


**Figure 3.13:** Phase Comparison of Theory and Experiment (1). Comparison of total reflection-phase (solid line) of the walls of the cavity, with the calculated values for  $m=1$  (squares) and  $m=2$  (circles). The defect structure is obtained by separating a 12 layer crystal from the half.

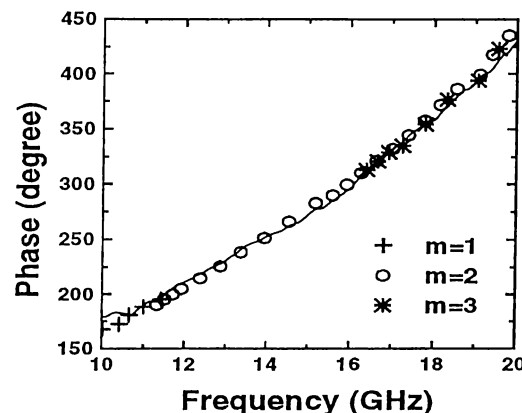


**Figure 3.14:** Phase Comparison of Theory and Experiment (2). Comparison of total reflection-phase (solid line) of the walls of the cavity, with the calculated values for  $m=1$  (crosses),  $m=2$  (circles), and  $m=3$  (stars). The separation length is increased further to observe  $m=3$  defect modes. The defect structure is generated so that the crystal on either side of the defect plane is symmetric.

For the second case, the crystal is symmetric with respect to the plane of the cavity, along the stacking direction, and the surface rods on either side of the cavity are therefore parallel to each other. So the total phase is obtained

by adding the reflection-phases of the two walls for same polarizations, which is the solid line in figure 3.14. The polarization vector  $\mathbf{e}$  of the incident EM wave is perpendicular to the surface rods on either side of the cavity. Double defects modes are also observed, where the secondary defect modes are shown as  $m=2$ . All of these graphs support the validity of the theory built in chapter 2. But as discussed earlier, since there are extra peaks in between the two consecutive modes, appearing with the change of angle of incidence, the theory still needs to be improved.

We also tried to investigate the reflection-magnitude properties of metallic crystals with defects, where a single rod, or every other rod from a single layer are removed. For such defect structures, it was hard to observe any reflection rejection at corresponding defect frequencies. Later, we measured the magnitude-reflection of the Fabry-Perot cavities. Surprisingly, we observed strong reflection rejection ratios for these defect structures. Figure 3.15 (a) shows the transmission and reflection spectra of an 8 layer crystal, which is separated 5 mm from the middle. The frequency of the defect mode appears to be around 17.5 GHz, with a Q-factor of the defect mode around 100, measured from the transmission. The transmission amplitude of the defect mode is equal to the incident field. On the other hand, maximum reflection rejection amplitude measured at the defect frequency is around 80 dB below the incident signal. This value may even be higher, but the noise level of our setup puts a limit for our measurements. The surprising thing in the reflection is the sharp drop of the reflected signal around the defect frequency. Figure 3.15 (b) shows the reflection around defect frequency in an extended scale.

We will return back to Fabry-Perot analogy to understand the situation. Using the  $E_c$  we have calculated in equation 2.1, we can write the reflected field  $E_r$  as:

$$E_r = r_1 E_i + j t_1 r_2 e^{-2j\beta L} E_c \quad (3.2)$$

where we did not consider the phase contributions of the mirrors. Inserting the

$E_c$  in equation 3.2, we get the ratio of the reflected field to the incident field as:

$$\frac{E_r}{E_i} = \frac{r_1 - r_2 e^{-2j\beta L}}{1 - r_1 r_2 e^{-2j\beta L}} \quad (3.3)$$

The special situation when the reflectivities of the mirrors are exactly equal cause the expression at the numerator of the equation 3.3 to become zero at resonance. In our case, where the reflectivities of the walls of the planar defect are equal, the net reflection coefficient cancels at defect frequency. So we observe the sharp drop at resonance in the reflection-amplitude.

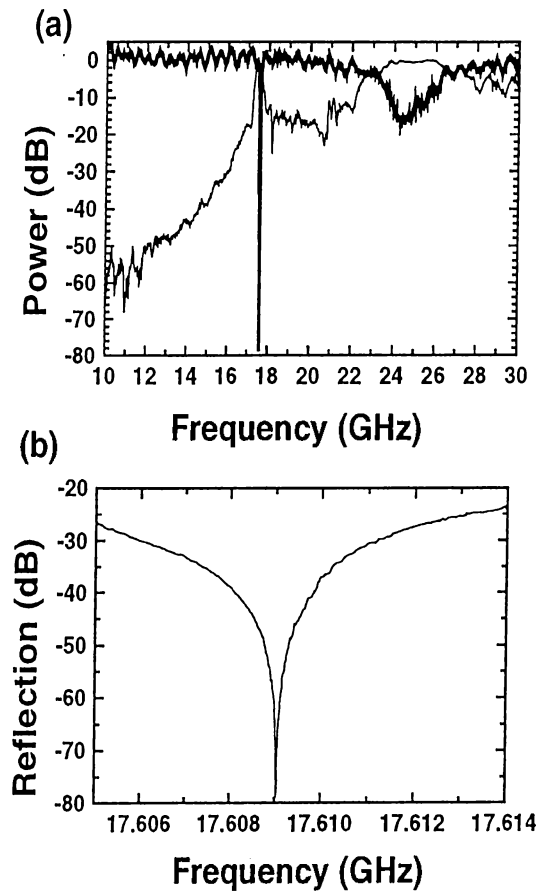


**Figure 3.15:** High reflection rejection from a defect structure.

(a) The reflection (thick solid line) and transmission (thin solid line) characteristics of an 8-layer st crystal with planar defect. (b) Reflection characteristics of the defect mode in an expanded scale.

# Chapter 4

## Resonant Detectors Inside Dielectric Photonic Crystals

Until now, we worked on the transmission and reflection properties of photonic crystals. We developed theories to understand defect formation, using the transmission and reflection information of the crystal. However, we have no idea on the characteristics of the field circulating inside the defect volume.

From the theory of Fabry-Perot resonant microcavities, we can deduce that the field inside the cavity is highly magnified for certain resonant wavelengths. Resonant cavity enhanced (RCE) detectors can be formed by placing the detector inside a Fabry-Perot resonant microcavity. This way, the detector benefits from the wavelength selectivity and the large increase of the resonant EM field introduced by the cavity.<sup>30</sup> In this chapter, we first go over the theory of the RCE detectors. Then, we try to simulate the RCE structure by inserting a monopole antenna inside the defect volume, and measure the enhanced field. A network analyzer and a powermeter are used for characterization. We also repeat the same experiments by connecting the monopole antenna to a multimeter, via a Schottky diode detector. Later on, we place the detector inside the cavity, and investigate the characteristics of the magnified field inside the defect.

## 4.1 The circulating intensity magnification

The Fabry-Perot analog defects we are dealing with can be considered as passive optical cavities.<sup>32</sup> In chapter 2, we studied the character of the circulating field intensity. In equation 2.2, we related the circulating signal inside the cavity to the incident signal outside the cavity. When the resonance condition is satisfied, the field intensity inside the cavity can become quite high. These correspond to the defect modes in photonic crystals. What happens to the intensity of the field inside the cavity can be clarified by giving a simple Fabry-Perot resonator example. We assume that the reflectivities of the mirrors are equal, that is  $r_1 = r_2 = r$ . At resonance condition, equation 2.2 reduces to:

$$\frac{E_c}{E_i} = \frac{jt}{1 - r^2} = \frac{j}{t} \quad (4.1)$$

where we used  $t = t_1 = t_2 = \sqrt{1 - r^2}$ , for lossless mirrors. So the ratio of the circulating field intensity to the incident intensity can be given as:

$$\frac{I_c}{I_i} = \left| \frac{1}{t} \right|^2 = \frac{1}{T} \quad (4.2)$$

where  $T = t_2$  is the power transmission of either end mirror. For example, with 99% reflecting mirrors, that is for  $r = 0.99$ , the power transmission becomes  $T = 0.01$ . So the circulating intensity becomes  $I_c = 100I_i$ . In other words, 1 unit of power incident on this cavity can build up a circulating power which is around 100 units of power travelling in each direction inside the cavity, as illustrated in figure 4.1.

To visualize the situation, the transmitted (a) and circulating (b) fields of such an optical resonator, as a function of  $2\beta L$ , is shown in figure 4.2. The calculations are made by the use of equation 2.5 for the circulating field intensity inside the cavity, and absolute square of the equation 2.12 for the transmitted field from the cavity. We assume that the cavity is lossless, and the reflection-phase factors of the mirrors are zero. The figure shows how amplitudes of the peaks get higher, when the reflectivities of the mirrors are increased from 68% to 98% for the circulating field. The Q factors also increase the same way as

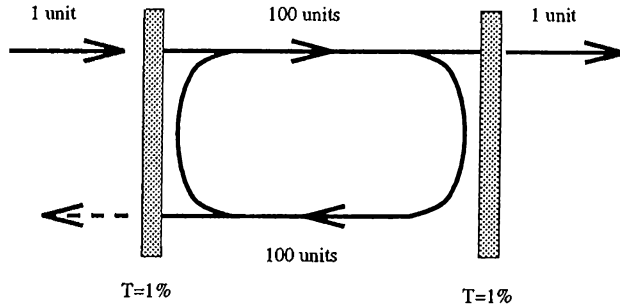


**Figure 4.1:** Magnification of the circulating signal.  
The field inside the passive resonant cavity is magnified 100 times.

expected from the equation 2.13.

As shown in figure 4.2, the circulating power can become much higher than the incident signal. But of course, due to the energy conservation principles, this energy can not be usefully extracted, continuously at least. However, RCE devices are able to use the properties of this magnified field for various applications.

We will continue our work by introducing an absorption region inside the cavity, as done for the case of RCE devices.<sup>30</sup> The model will simulate our detector inserted inside a planar type of defect. Now, we have to rewrite the equations for the forward travelling wave and backward travelling wave, and with a relative absorption coefficient of the absorption region  $\alpha$ . The electrical field component for the forward travelling wave  $E_f$  can be related to the incident field as:

$$E_f = \frac{t_1}{1 - r_1 r_2 e^{-\alpha d} e^{-j(2\beta L + \phi_1 + \phi_2)}} E_i \quad (4.3)$$

where  $d$  is the length of the absorption region. And the backward travelling wave can be related to forward travelling wave as:

$$E_b = r_2 e^{-\alpha d/2} e^{-j(\beta L + \phi_2)} E_f \quad (4.4)$$

Using the equations 4.3 and 4.4, we can calculate the magnitude of the absorbed field by the detector inside the cavity, normalized with respect to the absorbed incident field by the detector, as:

$$\eta = \left\{ \frac{1 + Re^{-\alpha d}}{1 - Re^{-\alpha d} \cos(2\beta L + \phi_1 + \phi_2) + R^2 e^{-2\alpha d}} \right\} (1 - R) \quad (4.5)$$

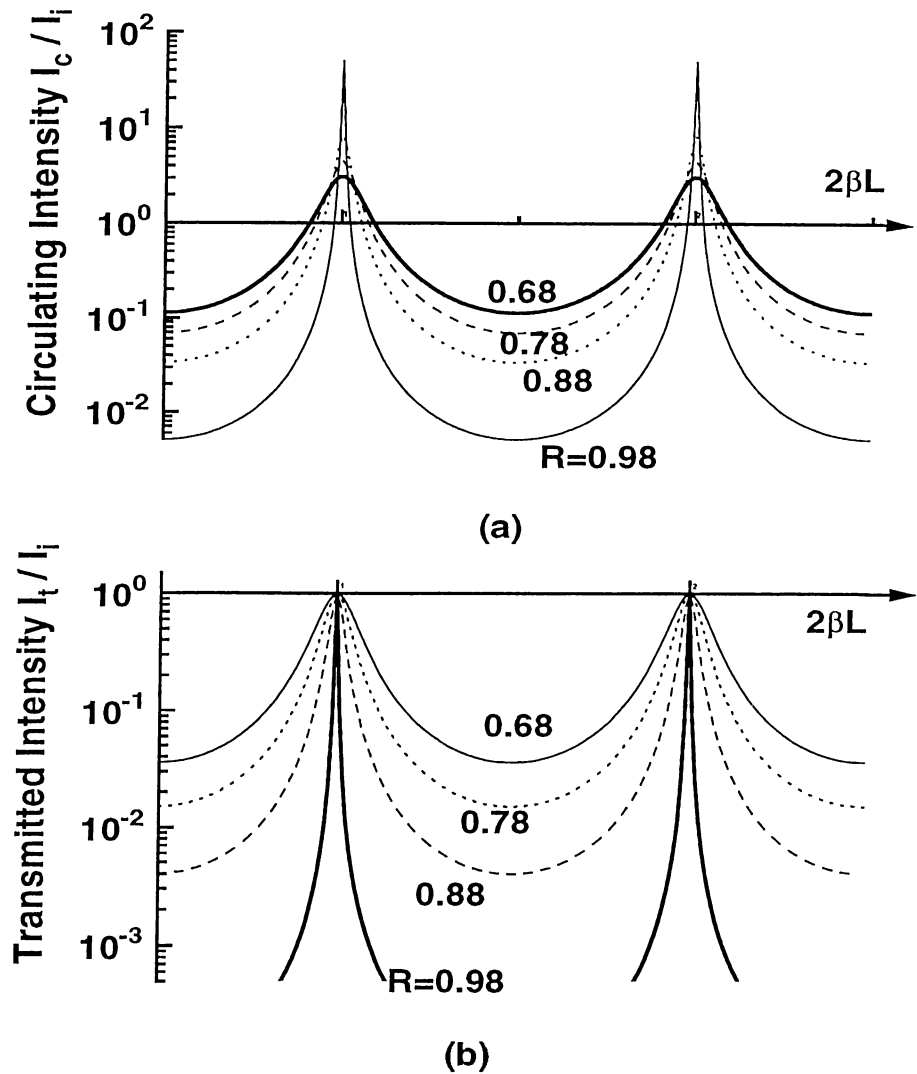


**Figure 4.2:** Fabry-Perot modeling

Circulating (a) and transmitted (b) power in an optical resonator, with mirror reflectivity  $R = R_1 = R_2$ , assuming no internal loss.<sup>32</sup>

where the reflectivities of the mirrors of the cavity are equal to  $R = r_1^2 = r_2^2$ . This  $\eta$  corresponds to the enhancement we are measuring. Figure 4.3 shows the magnification of the intensity as a function of  $2\beta L$  for the case where  $\alpha d = 0.9975$  and  $\phi_1 = \phi_2 = 0$ . The four curves correspond to the case of  $R=0.9975, 0.99, 0.97$

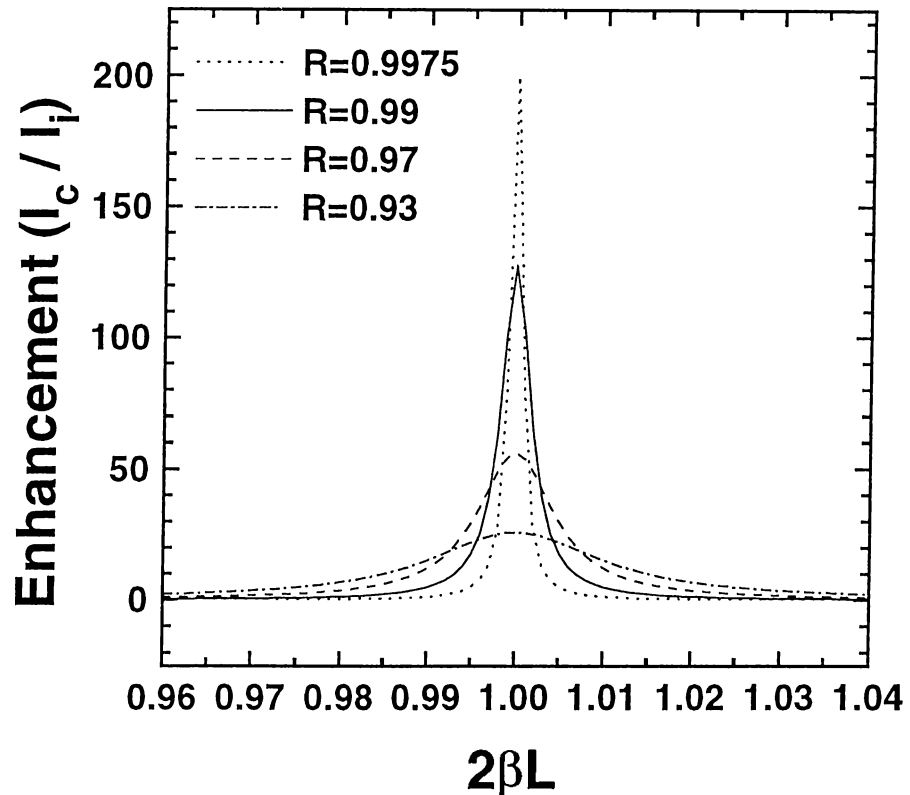


Figure 4.3: RCE modeling

Absorbed field enhancement by the detector inside an RCE device.

and 0.93. The highest reflectivity chosen corresponds to the reflectivities of 8-layer crystals, which are the walls of the planar defect for our case. So we are expecting an enhancement factor of 200 inside the planar defect structure.

## 4.2 Experimental setup

Figure 4.4 shows our experimental setup for enhancement measurements. The center conductor of a coaxial cable is used as the receiver antenna in our measurements. One edge of the cable is cleaved, and acted as a monopole antenna. The cleaved part is around 8 mm, an optimized length, which is long enough to

detect the signal, while short enough for minimal disturbance of the EM field inside the defect volume. The so formed monopole antenna is connected to a network analyzer, and a powermeter for cross check. The calibration is made with respect to the incidence signal, when there is no crystal. The transmission spectra is also taken in order to understand the effect of our receiver to the transmission characteristics of the defect.

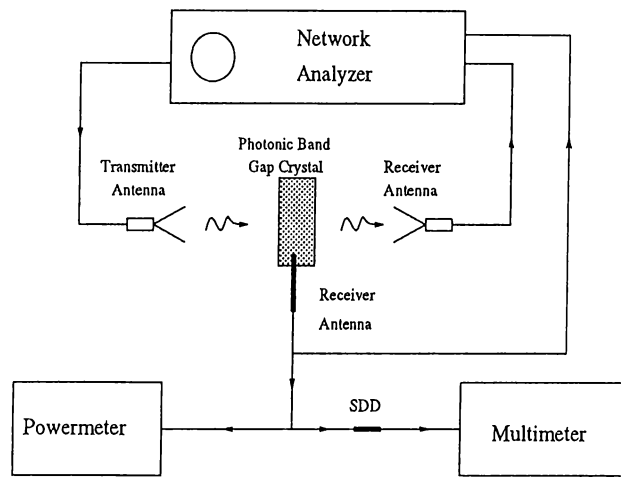


**Figure 4.4:** Experimental setup

Experimental setup for simultaneous measurements of transmission and field enhancement.

A few problems are faced while placing the probe inside the defect. The position of the probe has a significant impact on the characteristics of the detected EM wave. For certain positions of the probe, the detected amplitude of the peak is at its maximum, and for those positions, the transmission spectra of the mode is affected least. These are the positions for which our receiver couples least with the circulating field inside the cavity. This quite helps us in our experiments, since by this approach, the data will be taken for positions of the probe, where it least disturbs the system. It is also observed that, a probe placed in a regular photonic crystal does not affect the transmission spectra of the bulk crystal. Various kinds of defect structures are studied, where we minimize the effect of the probe to the EM field for each defect structure, by the cross check of the transmission spectra.

### 4.3 Measurements

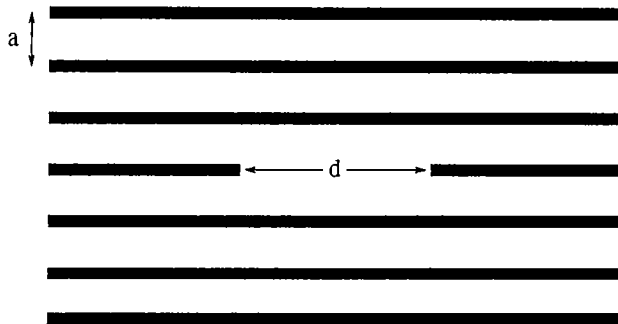


**Figure 4.5:** Defect Structure

Missing defect structure obtained by removing a part of the alumina rod.

The first defect type we studied is formed by removing some part of a single rod from a single layer. As shown in figure 4.5,  $d$  is the length of the removed part, and  $a$  is the lattice constant. The probe is inserted from one side of the crystal, and lies along the defect rod. The active part of the probe is placed inside the defect volume, and is parallel to the electric field polarization vector  $e$  of the incident EM wave. The peak amplitude of the defect mode measured from the probe is recorded as a function of the  $d/a$  ratio. As shown in table 4.1, the power observed inside the crystal increases, from 40% of the incident field at  $d/a=1$ , to an enhancement, which corresponds to 40 times of the incident field at  $d/a=8$ . The quality factors observed are at the order of 1000. Figure 4.6 shows the transmission spectra of a 16-layer crystal, where the 8th layer of the crystal is chosen as the defect layer, for the case  $d/a=8$ . Figure 4.7 shows the magnitude of the circulating field intensity obtained by our monopole antenna type receiver connected to the network analyzer. From both plots, we can see that the frequency of the localized mode is at 12.2 GHz. The transmission amplitude is 15.7 dB below the incident signal, with a Q-factor of 1400. The circulating field peak amplitude, on the other hand, is 15 times of the incident field, with a Q-factor of 1100.

We continue our work with Fabry-Perot type of cavities, which are planar defects in our case. Placing our probe inside such defects, we approach one step

d/a	Frequency GHz	Peak Amplitude (dB)
1	11.96	-4.0
2	12.37	-0.5
3	12.18	5.49
5	12.28	9.6
8	12.18	11.97

**Table 4.1:** The change of enhanced power as the d/a ratio of the defect is increased. No significant change in the frequency is observed.

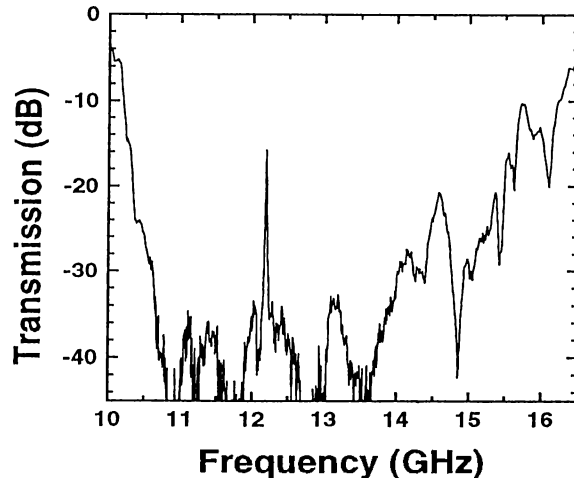


**Figure 4.6:** Transmission spectra of a defect mode  
Transmission spectra of a defect of the form shown in figure 4.5 with d/a=8

further to the RCE device model, where probe acts as the absorption region introduced into the cavity. This allows us to study the characteristics of the circulating EM fields inside planar defects. High values of enhancement are achieved for these structures, as expected from the RCE theory explained earlier. A 16-layer crystal is separated from the middle with a separation width of 7 mm. We then place the monopole antenna inside the defect volume, and measure the magnitude of the EM field by different methods. As shown in figure 4.8, the amplitude of the circulating field is characterized by a network analyzer (thick solid line), and the cross-check is made by a powermeter (thin solid line). The

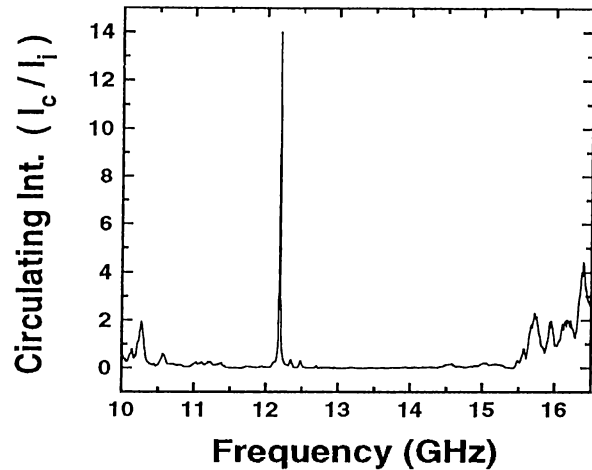


**Figure 4.7:** Power enhancement of a defect mode  
The magnified power inside a defect with  $d/a=8$

antenna is then connected to a multimeter for voltage reading, via a Schottky diode detector, as shown in setup figure 4.4. Figure 4.8 shows the measured amplitude of the circulating field (dotted line) obtained by the detector. All three measurements yield a peak signal at 12.32 GHz, 23 dB above the incident signal, corresponding to an enhancement factor of 200. The transmission peak amplitude of this defect mode is at -10 dB (as shown in figure 2.9 in chapter 2). Since the attenuation of 8-layer crystal is around 33 dB around 12 GHz (see figure 2.8) a -10 dB peak intensity obtained from the transmission corresponds to  $-10 + 33 = 23$  dB power traveling inside the cavity. This quite agrees with the 23 dB enhancement measured for this structure. This value also agrees well with the RCE model, for the case where we assumed the reflectivities of the mirrors of the cavity as high as the reflectivities of our walls of the cavity (thick solid line of figure 4.3). We then place the detector inside the cavity, which exactly simulates an RCE detector, for which the detector is the absorption region itself. However, the enhancements obtained were lower. The maximum enhanced power we measured is around 100 times that of the incident signal.

Later on, we tried to minimize the loss associated with the leakage along the

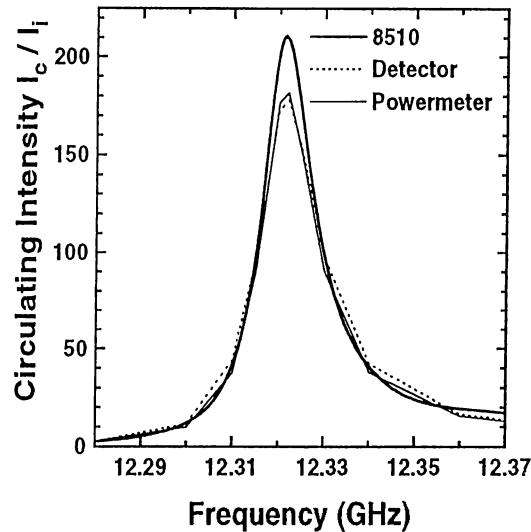


**Figure 4.8:** Enhancement of the field inside a planar defect.

The enhancement data obtained by the network analyzer (thick solid line), by powermeter (thin solid line), and by the Schotky diode detector (SDD) connected to a multimeter (dotted line).

plane of the cavity. Since our incident wave is not perfectly aligned parallel to the surface normal of the cavity, some portion of the EM waves may leak out of the cavity through waveguiding, and thus contribute to loss. So we try to increase the enhancement further by blocking the four sides of the planar defect, that is by introducing a box like cavity inside the crystal. This way, the field radiated out from the sides of the planar defect will be minimized, and the circulating field will be trapped inside the cavity. The dimensions of the cavity we investigate is  $m \times m$  along the plane perpendicular to the stacking direction, where we change the  $m$  value from  $a$  to  $6a$ , for  $a$  being the center to center separation of the rods, which is 1.12 cm. The cavity is 0.64 cm thick along the stacking direction, which is the thickness of a 2 layer crystal. The total crystal under investigation is 16 layers thick, where the 8<sup>th</sup> and 9<sup>th</sup> layers are chosen as the defect layers. However, the experiments do not reveal the expected enhancement for box-like defects. The highest enhanced power is achieved when the defect is a complete

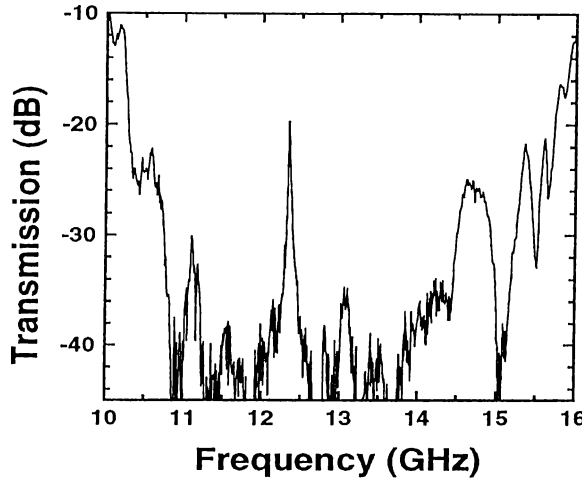


**Figure 4.9:** Transmission spectra from a box-like cavity.  
Transmission of a crystal with a box-like cavity obtained when the probe is inside the cavity.

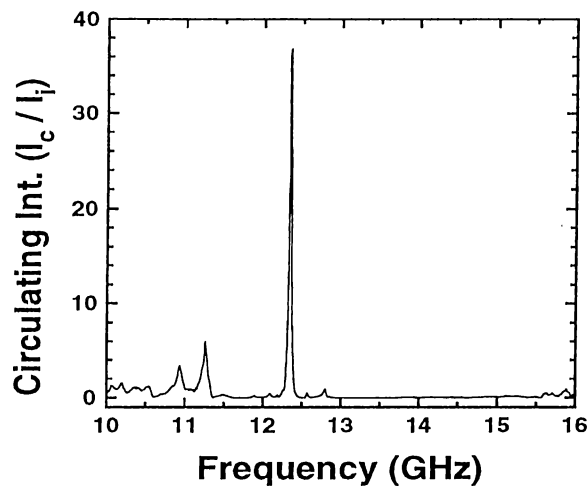


**Figure 4.10:** Circulating intensity magnification inside a box like cavity (1).  
The data is obtained by the probe connected to the network analyzer.

planar defect. In the box-type of cavity, the EM waves do not only circulate between two walls. We think that, the magnification of the field is distorted by the side-wall reflections. The peak amplitude of the defect mode increases as we

increase the size of the cavity by increasing  $m$ , and is equal to the value of the full planar defect, when  $m$  is 6. Figure 4.9 shows the transmission amplitude characteristics of the defect mode, for the case  $m=4a$ . The peak amplitude is around -20 dB below the incident signal, at a defect frequency of 12.37 GHz. As shown in figure 4.10 the enhanced power for the same structure is 37 times that of the incident signal, which is measured by the probe connected to the network analyzer. The transmission spectra shown in figure 4.9 is taken when the probe is inside the defect for the enhancement measurement. When we take out the probe, we observe no significant change in the transmission spectra. This also shows that the disturbance introduced by the absorption of the probe is negligible.

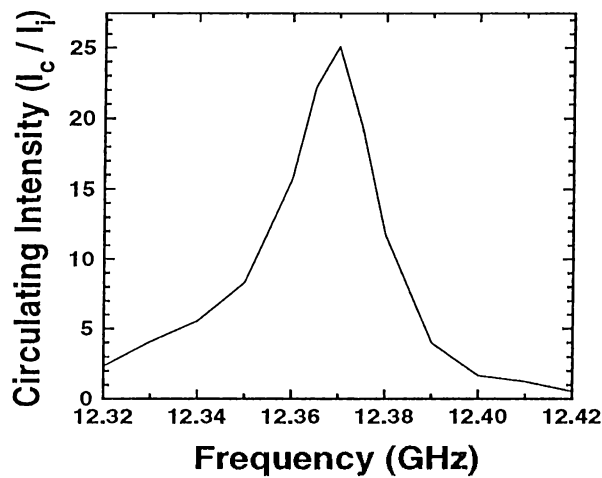


**Figure 4.11:** Circulating intensity magnification inside a box like cavity (2). The data is obtained by a Schottky diode detector placed inside the cavity, and connected to a voltmeter.

Finally, we placed the detector inside the box-like cavity, and performed the experiment again for the case of  $m=4a$ . Figure 4.11 shows the magnification of the field around defect frequency in an expanded frequency scale. This time, the amplitude of the peak is measured to be 25 times that of the incident signal, which is also lower than the previously obtained value of 40. This may arise from

the fact that the detector is not a suitable absorber for the detection of the field, or being grater in size than the probe, it may be distorting the field. Although the performance of the resonant detector is slightly limited, when compared to the measurements done with the network analyzer, our experiments still reveal the basic characteristics of the resonant cavity detector. These detectors may be quite useful in applications requiring increased sensitivity.

# Chapter 5

## Conclusions

In this thesis work, we investigated the reflection and transmission properties, and defect characteristics of the dielectric and metallic based photonic crystals.

First, we examined the reflection properties of a layer-by-layer dielectric-based photonic crystal. Strong polarization dependence were observed for the phase of the reflected waves. We have developed a Fabry-Perot model for planar defect structures, and compared the predicted reflection-phase properties with the experimentally measured ones. The agreement between the prediction and the experiment was very good, confirming the validity of the Fabry-Perot model used for the planar defect structures. To our knowledge, these were the first reported reflected-phase measurements of photonic crystals in scientific literature.

Using the Fabry-Perot analogy, we also developed a simple model for the Q-factors of the defect modes. The transmission intensity of a single wall of the cavity was found to be inversely proportional to the Q-factor of the defect mode of that frequency. The highest Q-factor obtained for planar type defects was around 5300. We also simulated the transmission characteristics of the crystals with planar defects, and the resulting agreement in between was also good.

We continued our work with layer-by-layer metallic photonic crystals. The transmission characteristics of st and fct type crystals were studied. The attenuation per layer was about 7-8 dB, which was quite high when compared to 3-4 dB attenuation per layer that can be obtained from a dielectric based photonic

crystal. Later on, we compared the defect characteristics for both st and fct type crystals. St based metallic defect structures were found to be superior to fct based metallic defect structures in terms of peak amplitude and the maximum achievable Q-factor. Defect modes created by removing rods resulted in high peak transmission (80%), and high Q-factors (1740). Our measurements were in good agreement with the theoretical expectations. The Q-factors of the planar type of defects were higher (2250). To our knowledge, our defect measurements correspond to the highest Q-factors reported for metallic photonic crystals in scientific literature.

We also performed the reflection measurements for the metallic photonic crystals. We again observed a similar polarization dependence for the phase of the reflected waves, but the phase had much smaller dispersion than that of the dielectric-based photonic crystals. This reflection-phase information was used to predict the frequency of the defect mode of Fabry-Perot type of cavity. We observed that the model built for the dielectric-based photonic crystals also holded for the metallic photonic crystals. The reflection-magnitude characteristics of the crystals with defects were also investigated. For planar type of defects, strong reflection rejection ratios at defect frequencies were observed, which is explained by the Fabry-Perot cavity theory.

Finally, we tried to measure the magnified circulating intensity of the localized EM field inside the defect volume. We used the theory of passive optical cavities and resonant cavity enhanced devices to understand the concept of magnification. Using a monopole antenna which is placed inside the defect as a receiver, high values of enhanced power are observed, which were of the order of 200 times of the incident signal. We obtained the same order of enhancement when we connect the receiver to a multimeter, via a Schottky diode detector. Later on, we tried to minimize the loss associated with the leakage along the plane of the cavity, by blocking the four sides of the cavity. However, the magnification of the field was distorted by the side-wall reflections. The resulting enhancements with respect to the incident signal were around 40, lower than the enhancement obtained from planar defects. Later on, we performed the measurements by placing the

Schottky diode detector inside the defect volume. The achieved enhancements were around 100 for planar type defects, and 25 for box-type of cavities. To our knowledge, this is the first observation of resonant cavity enhanced detectors in photonic crystals.

We plan to continue our work with the investigation of the waveguide nature of photonic crystals. The guidance of the EM wave through the planar type of defects will be studied, for both dielectric and metallic based photonic crystals. We expect that, the understanding gained from waveguides would be helpful in lowering the size of integrated optic circuits (as described in chapter 1), if the dimensions of photonic crystals can be lowered to reach optical frequencies.

The other goal is to lower the dimensions of the layer-by-layer photonic crystal by silicon micro-machining techniques. By using special silicon thinning methods and double etching the wafers on both surfaces, we plan to build structures with photonic band gaps located at frequencies as high as 3 THz. We also expect that this layer-by-layer structure will be useful at even smaller scales for the eventual goal of fabricating photonic gap structures at infrared and optical frequencies.

# Bibliography

- [1] E. Yablonovitch, "Inhibited Spontaneous Emission in Solid-State Physics and Electronics," *Phys. Rev. Lett.* **58**, 2059 (1987).
- [2] S. John, "The Localization of Light," NATO Advanced Science Institute on *Localization and Propagation of Classical Waves in Random and Periodic Structures*, held May 1992, Crete, GREECE, Plenum Publ. Corp. (1993).
- [3] P.R. Villeneuve, S. Fan, J.D. Joannopoulos, K.Y. Lim, G.S. Petrich, L.A. Kolodziejski, and R. Reif, "Air-Bridge Microcavities," *Appl. Phys. Lett.* **67**, 167 (1995).
- [4] P.L. Gourley, J.R. Wendt, G.A. Vawter, T.M. Brennan, and B.E. Hammons, "Optical Properties of Two Dimensional Photonic Lattices Fabricated as Honeycomb Nanostructures in Compound Semiconductors," *Appl. Phys. Lett.* **64**, 687 (1994).
- [5] J.P. Dowling, M. Scalora, M.J. Bloemer, and J.M. Bowden, "The Photonic Band Edge Laser: A New Approach to Gain Enhancement," *Appl. Phys. Lett.* **75**, 1896 (1994).
- [6] E.R. Brown, C.D. Parker, and E. Yablonovitch, "Radiation Properties of a Planar Antenna on a Photonic-Crystal Substrate," *J. Opt. Soc. Am. B* **10**, 404 (1993).
- [7] E.R. Brown, and O.B. McMahon, "High Zenithal Directivity from a Dipole Antenna on a Photonic Crystal," *Appl. Phys. Lett.* **68**, 1300 (1996).

- [8] C.J. Maggiore, A.M. Clogston, G. Spalek, W.C Sailor, and F.M. Mueller, "Low-Loss Microwave Cavity Using Layered-Dielectric Materials," *Appl. Phys. Lett.* **64**, 1451 (1994).
- [9] D.R. Smith, S. Shultz, N. Kroll, M. Sigalas, K.M. Ho, and C.M. Soukoulis, "Experimental and Theoretical Results for a Two-Dimensional Metal Photonic Band-Gap Cavity," *Appl. Phys. Lett.* **65**, 645 (1994).
- [10] E. Yablonovitch, "Photonic Band-Gap Structures," *J. Opt. Soc. Am. B* **10**, 283 (1993).
- [11] R.G. Hulet, E.S. Hilfer, and D. Kleppner, *Phys. Rev. Lett.* **53**, 2137 (1985)
- [12] Y. Yamamoto, S. Machida, and W.H. Richardson, "Photon Number Squeezed States in Semiconductor Lasers," *Science* **55**, 1219 (1992).
- [13] K.M. Ho, C.T. Chan, and C.M. Soukoulis, "Existence of a Photonic Band Gap in Periodic Structures," *Phys. Rev. Lett.* **65**, 3152 (1990).
- [14] E. Yablonovitch, and T.J. Gmitter, "Photonic Band Structure: The Face Centered-Cubic Case," *Phys. Rev. Lett.* **63**, 1950 (1989).
- [15] K.M. Leung, and Y.F. Liu, "Full Vector Wave Calculation of Photonic Band Structures in Face-Cubic-Centered Dielectric Media," *Phys. Rev. Lett.* **65**, 2646 (1990).
- [16] Z. Zhang, and S. Satpathy, "Electro-Magnetic wave Propagation in Periodic Structures: Bloch Wave Solutions of Maxwell's Equations," *Phys. Rev. Lett.* **65**, 2650 (1990).
- [17] E. Yablonovitch, and K.M. Leung, "Photonic Band Structure: Non-Spherical Atoms in the Face-Centerd Case," *Physica B* **175**, 81 (1991).
- [18] E. Özbay, A. Abeyta, G. Tuttle, M. Tingides, R. Biswas, C.T. Chan, C.M. Soukoulis, and K.M. Ho, "Measurement of a Three-Dimensional Photonic Band Gap in a Crystal Structure Made of Dielectric Rods," *Phys. Rev. B* **50**, 1945 (1994).

- [19] E. Özbay, E. Michel, G. Tuttle, R. Biswas, M. Sigalas, and K.M. Ho, "Micromachined Millimeter-Wave Photonic Band-Gap Crystals," *Appl. Phys. Lett.* **64**, 2059 (1994).
- [20] E. Özbay, E. Michel, G. Tuttle, R. Biswas, M. Sigalas, K.M. Ho, J. Bostak and D.M. Bloom, "Terahertz Spectroscopy of Three-dimensional Photonic Band-Gap Crystals," *Opt. Lett.* **19**, 951 (1994).
- [21] E. Özbay, E. Michel, G. Tuttle, R. Biswas, K.M. Ho, J. Bostak and D.M. Bloom, "Double-etch Geometry for Millimeter-Wave Photonic Band-Gap Crystals," *Appl. Phys. Lett.* **65**, 1617 (1994).
- [22] E. Yablonovitch, T.J. Gmitter, R.D. Meade, A.M. Rappe, K.D. Brommer, and J.D. Joannopoulos, "Donor and Acceptor Modes in Photonic Band Structure," *Phys. Rev. Lett.* **67**, 3380 (1991).
- [23] E. Özbay, G. Tuttle, M. Sigalas, C.M. Soukoulis, and K.M. Ho, "Defect Structures in a Layer-by-Layer Photonic Band-Gap Crystal," *Phys. Rev. B* **51**, 13961 (1995).
- [24] S.D. Cheng, R. Biswas, E. Özbay, S. McCalmont, G. Tuttle, and K.M. Ho, "Optimized Dipole Antennas on Photonic Band Gap Crystals," *Appl. Phys. Lett.* **67**, 3399 (1995)
- [25] J.D. Joannopoulos, "An Introduction to Photonic Crystals," NATO Advanced Science Institute on *Photonic Band Gaps and Applications*, held June 1995, Crete, GREECE, Plenum Publ. Corp. (1995).
- [26] M.M. Sigalas, C.T. Chan, K.M. Ho, and C.M. Soukoulis, "Metallic Photonic Band-Gap Materials," *Phys. Rev. B* **52**, 11744 (1995).
- [27] S. McCalmont, M. Sigalas, G. Tuttle, and K.M. Ho, "A Layer-by-Layer Metallic Photonic Band Gap Structure," *Appl. Phys. Lett.* **68**, 2759 (1996).
- [28] D.F. Sievenpiper, M.E. Sickmiller, and E. Yablonovitch, "3-D Wire Mesh Photonic Crystals," *Phys. Rev. Lett.* **76**, 2480 (1996).

- [29] E. Özbay, and B. Temelkuran, "Reflection Properties and Defect Formation in Photonic Crystals," *Appl. Phys. Lett.* **69**, 743 (1996).
- [30] M.S. Ünlü, "Resonant Cavity Enhanced Photonic Devices," *J. Appl. Phys.* **78**, 1 (1995).
- [31] K.M. Ho, C.T. Chan, C.M. Soukoulis, R.Biswas, and M.Sigalas, "Photonic Band Gaps in Three Dimensions: New Layer-by-Layer Periodic Structures," *Solid State Commun.* **89**, 413 (1994)
- [32] A.E. Siegman, *Lasers*, University Science Books (1986)
- [33] E. Özbay, G. Tuttle, J.S. McCalmont, M.Sigalas, R.Biswas, C.M. Soukoulis, and K.M. Ho, "Laser Micromachined Millimeter-Wave Photonic Band-Gap Cavity Structures," *Appl. Phys. Lett.* **67**, 1969 (1995).
- [34] J.B. Pendry and A. MacKinnon, "Calculation of Photon Dispersion Relation," *Phys. Rev. Lett.* **69**, 2772 (1992); J.B. Pendry, "Photonic Band Structures," *J. Mod. Opt.* **41**, 209 (1994).
- [35] M.M. Sigalas, C.M. Soukoulis, C.T. Chan, and K.M. Ho, "Electromagnetic-Wave Propagation Through Dispersive and Absorptive Photonic-Band-Gap Materials," *Phys. Rev. B* **49**, 11080 (1994).